

# Mineral-melt partitioning of redox-sensitive elements

Antony D Burnham<sup>1</sup>, Guil Mallmann<sup>1</sup>, and Raul O C Fonseca<sup>2</sup>

<sup>1</sup>Australian National University

<sup>2</sup>Ruhr-University Bochum

November 23, 2022

## Abstract

Elements with variable valence state (i.e. redox-sensitive) often show contrasting mineral/melt partition coefficients as a function of oxygen fugacity ( $fO_2$ ) in magmatic systems. This is because trace-element incorporation into crystal lattices depends on the charge, size, and crystal-field stabilization energy of atoms, all of which differ greatly between oxidized and reduced species of the same element. This has two critical implications: (1) petrologic/ geochemical modelling of partitioning behavior of redox-sensitive trace-elements in magmatic systems requires some knowledge of their oxidation state, and (2) the oxidation state of magmatic systems may be inferred from partitioning relations of redox-sensitive trace elements preserved in mineral and melt phases of rapidly cooled magmas. The advantage of this oxybarometric approach is that mineral/melt partitioning relations are not sensitive to late stage degassing, charge-transfer on quenching, or surficial alteration. In this chapter we discuss the theoretical treatment of experimental mineral/melt partitioning data of redox-sensitive trace elements, and review aspects concerning the partitioning behavior of well-known redox-sensitive elements, including transition metals (Ti, V, Cr, Fe), rare earth elements (Ce, Eu), U, and siderophile elements (Mo, W, Re, and platinum group elements) under planetary magmatic  $fO_2$  conditions.

# Mineral-melt partitioning of redox-sensitive elements

## Running head: Partitioning of redox-sensitive elements

Keywords: Oxygen fugacity, Partition coefficients, Multivalent elements, Magmatism

G. Mallmann<sup>1\*</sup>, A.D. Burnham<sup>1</sup>, R.O.C. Fonseca<sup>2</sup>

<sup>1</sup> Research School of Earth Sciences, Australian National University, Canberra ACT 2601, Australia

\*(corresponding author)

<sup>2</sup> Institute of Geology, Mineralogy and Geophysics Ruhr-University Bochum, Universitätsstr. 150, 44780 Bochum, Germany

### Abstract

Elements with variable valence state (i.e. redox-sensitive) often show contrasting mineral/melt partition coefficients as a function of oxygen fugacity ( $fO_2$ ) in magmatic systems. This is because trace-element incorporation into crystal lattices depends on the charge, size, and crystal-field stabilization energy of atoms, all of which differ greatly between oxidized and reduced species of the same element. This has two critical implications: (1) petrologic/geochemical modelling of partitioning behavior of redox-sensitive trace-elements in magmatic systems requires some knowledge of their oxidation state, and (2) the oxidation state of magmatic systems may be inferred from partitioning relations of redox-sensitive trace elements preserved in mineral and melt phases of rapidly cooled magmas. The advantage of this oxybarometric approach is that mineral/melt partitioning relations are not sensitive to late stage degassing, charge-transfer on quenching, or surficial alteration. In this chapter we discuss the theoretical treatment of experimental mineral/melt partitioning data of redox-sensitive trace elements, and review aspects concerning the partitioning behavior of well-known redox-sensitive elements, including transition metals (Ti, V, Cr, Fe), rare earth elements (Ce, Eu), U, and siderophile elements (Mo, W, Re, and platinum group elements) under planetary magmatic  $fO_2$  conditions.

### 1. Introduction

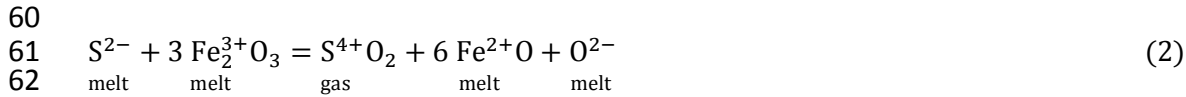
Although it is possible to determine valence-state ratios of redox-sensitive trace elements in natural and synthetic silicate glasses using techniques such X-ray absorption spectroscopy (e.g. Sutton and Newville, 2014), it may be challenging to relate these ratios to the oxygen fugacity ( $fO_2$ ) of a silicate melt. This is because many elements exchange electrons with Fe, the most abundant redox-sensitive element in most magmas, upon quenching. For example, a mid-ocean ridge basaltic (MORB) melt at 1400 °C equilibrated at  $fO_2$  equivalent to FMQ-1.7 (i.e. 1.7 log units below the  $fO_2$  defined by the fayalite-magnetite-quartz buffer at the same temperature) has  $Cr^{2+}/\Sigma Cr \sim 0.5$  (where  $\Sigma Cr = Cr^{2+} + Cr^{3+}$ ), but upon quenching to a glass all the  $Cr^{2+}$  is converted to  $Cr^{3+}$  by reaction with  $Fe^{3+}$  (Berry et al., 2003):



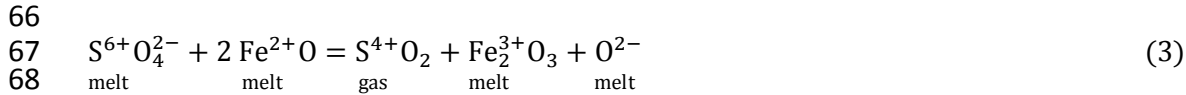
Similar reactions with Fe have been documented for Eu and Ce (Burnham and Berry, 2014; Burnham et al., 2015), but because they require only the transfer of electrons, they are probably unavoidable. Consequently, valence-state ratios of trace elements in natural Fe-bearing glasses may not be representative of their high-temperature melt chemistry.

Provided that these elements are only present at low abundances relative to Fe, the exchange minimally affects the  $Fe^{3+}/\Sigma Fe$  (where  $\Sigma Fe = Fe^{2+} + Fe^{3+}$ ) of the magma. However, this ratio can still be affected by degassing of volatile species (e.g. Burgisser and Scaillet, 2007;

55 Mathez, 1984; Sato, 1978) as well as surficial oxidation (e.g. Rhodes and Vollinger, 2005). Sulfur  
 56 degassing appears to be particularly important in the Earth because of the strong capacity of S  
 57 to either reduce or oxidize Fe depending on the initial oxidation state of the magma (e.g. de  
 58 Moor et al., 2013; Moussallam et al., 2016). For instance, the  $\text{Fe}^{3+}/\Sigma\text{Fe}$  of reduced magmas,  
 59 where  $\text{S}^{2-}$  (sulfide) is the dominant melt species, may be further reduced upon degassing of  $\text{SO}_2$ :



63  
 64 whereas the  $\text{Fe}^{3+}/\Sigma\text{Fe}$  of oxidized magmas, where  $\text{S}^{6+}$  (sulfate) is the dominant melt species,  
 65 may be further oxidized upon degassing of  $\text{SO}_2$ :



69  
 70 While potentially significant in their own right, such effects obscure the primary  
 71 magmatic redox characteristics. In contrast, high-temperature distributions of trace elements  
 72 between minerals and melts (i.e. partitioning relations) are readily preserved in rocks that have  
 73 cooled at moderate or rapid rates, and hence allow the petrologist to ‘see’ melt chemistry that  
 74 more accurately reflects the properties of the source of a magma. Furthermore, analysis of trace  
 75 elements in minerals and glasses is readily achieved using benchtop equipment, unlike some  
 76 spectroscopic techniques such as XANES that require access to the handful of suitably-equipped  
 77 synchrotron beamlines worldwide. Hence, mineral/melt partitioning allows more convenient  
 78 insights into the redox states of magmas.

79  
 80 To derive viable oxybarometers from mineral/melt partitioning, experimental data and  
 81 a thermodynamic framework are required. Experimental equipment, such as gas-mixing tube  
 82 furnaces, allows access to  $\sim 25$  log units of  $f\text{O}_2$  at 1400 °C; from 10 log units below the iron-  
 83 wüstite buffer (IW-10) to six log units above the hematite-magnetite buffer (HM+6). For  
 84 several redox-sensitive elements this is sufficient to encompass the entire transition from one  
 85 valence state to another (where the redox reaction involves the exchange of 1 electron, such as  
 86  $\text{Cr}^{2+}$  to  $\text{Cr}^{3+}$ , the transition occurs over 16 log units, whereas for elements whose redox  
 87 transition involves the exchange of 8 electrons, such as  $\text{S}^{2-}$  to  $\text{S}^{6+}$ , the transition occurs over 2 log  
 88 units). This allows the partitioning behavior of the end-members to be determined.  
 89 Nevertheless, in several cases it is not feasible to do this. For instance, where one valence state  
 90 is highly volatile (e.g.  $\text{Cr}^{6+}$  or  $\text{Mo}^{6+}$ ), or where an intermediate valence state always exists  
 91 alongside a higher or lower valence state (e.g.  $\text{V}^{3+}$ ,  $\text{V}^{4+}$  and  $\text{U}^{5+}$ ), or when extreme redox  
 92 conditions necessary to constrain the partitioning behavior of a valence state alone cannot be  
 93 achieved in the laboratory. In such cases, it may be necessary to model the expected behavior of  
 94 a valence state.

95  
 96 Lattice strain theory has become one of the fundamental concepts for understanding  
 97 trace element partitioning into minerals (Blundy and Wood, 1994; Wood and Blundy, 2003).  
 98 The essence of the theory is that substitution of a trace element  $i$  onto a cation site in a crystal  
 99 lattice is energetically neutral if the substituent ion has the same ionic radius ( $r_i = r_0$ ) and  
 100 charge as the ion it replaces, resulting in a partition coefficient  $D_0$ . Where its ionic charge and/or  
 101 radius differs, electrostatic work is done in repelling or attracting the adjacent anions (usually  
 102 oxygen), and this work results in the trace element being less compatible than the one with  
 103 optimal charge and radius, i.e.  $D_i < D_0$ . The dependence of  $\log D_i$  on  $r_i$  is approximately  
 104 parabolic;  $D_0$  likewise has a quadratic dependence on atomic number,  $Z$  (Fig. 1). These two  
 105 controlling variables are the reason that the various valence states of an element can have  
 106 striking differences in their partitioning behavior. Consider the removal of an electron from  
 107  $\text{Eu}^{2+}$ :

108



110

111 which not only increases the charge of the cation, but also (because of its higher effective  
112 nuclear charge) cause a contraction of the electronic orbitals, resulting in a decrease in ionic  
113 radius. This same principle applies to other major and trace elements capable of more than one  
114 valence state. As charge and ionic radius are principal controls on partitioning, it is almost  
115 inevitable that different valence states of an element will behave like different elements.  
116 Routine analytical techniques do not measure the speciation of redox-sensitive elements, which  
117 are usually reported as total concentrations without regard for the important differences  
118 between their valence states.

119

120 There are however challenges in the application of lattice strain theory to predict  
121 partition coefficients. These come mainly from crystal field effects and from the multitude of  
122 substitution mechanisms that are possible for a single cation in mineral sites.

123

124 Furthermore, there are important crystal-chemical implications for the fact that  
125 different valence states, such as  $\text{Cr}^{2+}$  and  $\text{Cr}^{3+}$ , behave like different elements. Crystals must  
126 have an overall neutral charge, hence when  $\text{Cr}^{2+}$  substitutes for  $\text{Mg}^{2+}$  in olivine, this criterion is  
127 observed, with the simple substitution  $\text{Mg}^{2+} \leftrightarrow \text{Cr}^{2+}$  with the endmember  $\text{Cr}^{2+}$ -olivine forming  
128 according to the reaction:

129



131 melt melt olivine

132

133 which, because forsterite ( $\text{Mg}_2\text{SiO}_4$ ) saturation requires  $2\text{MgO} + \text{SiO}_2$  and hence a fixed  
134 relationship between the activities of  $\text{SiO}_2$  and  $\text{MgO}$ , can equivalently be written:

135

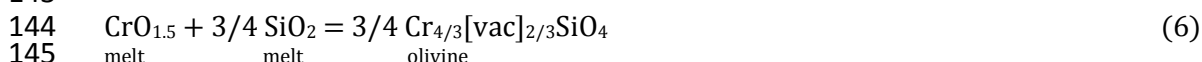


137 melt olivine. melt olivine

138

139 However, in order to substitute  $\text{Cr}^{3+}$  into the olivine structure, accommodation must be made  
140 for the difference in charge. One possibility involves the creation of vacancies [vac] on the  
141 octahedral site:  $2 \text{Mg}^{2+} \leftrightarrow 4/3 \text{Cr}^{3+} + 2/3[\text{vac}]$ . The reaction for formation of the corresponding  
142 endmember component is:

143



145 melt melt olivine

146

147 Another possibility involves coupled substitution with Al and Si on the tetrahedral site:  $\text{Mg}^{2+} +$   
148  $\text{Si}^{4+} \leftrightarrow \text{Cr}^{3+} + \text{Al}^{3+}$ . The reaction for formation of the corresponding endmember component is:

149



151 melt melt olivine olivine melt

152

153 Yet a third is tied to the incorporation of water:

154



156 melt melt melt olivine

157

158 It can be seen from Equations 5-8, that these different substitutions each have their own  
159 dependence on the activity of  $\text{SiO}_2$ , and some additionally depend on the activities of  $\text{Al}_2\text{O}_3$  and  
160  $\text{H}_2\text{O}$ . Furthermore, other components in the melt (e.g.  $\text{CaO}$ ) affect the activity coefficients of  $\text{CrO}$   
161 and  $\text{CrO}_{1.5}$ , and accordingly the transition between  $\text{Cr}^{2+}$  and  $\text{Cr}^{3+}$  and their partition coefficients  
162 are also sensitive to melt composition (Berry et al., 2006). Consequently, the examples of  
163 partition coefficients quoted in this review should be taken as illustrative, rather than definitive.



209 where  $K'_{10} = K_{10} / (\gamma_{M^{(x+n)^+}O_{(x+n)/2}} / \gamma_{M^{x^+}O_{x/2}})$  and the values in square brackets represent  
 210 concentrations converted from mole fractions (note that the conversion factor from mole  
 211 fractions to concentration cancels out between the numerator and denominator in the  
 212 quotient). Taking the logarithm of this equation and re-arranging gives:  
 213

$$\log \left( \frac{[M^{(x+n)^+}O_{(x+n)/2}]}{[M^{x^+}O_{x/2}]} \right) = \frac{n}{4} \log fO_2 + \log K'_{10} \quad (13)$$

214  
 215

216 In the case where only two valence states are possible in the melt, by defining  $\sum M = M^{x^+} +$   
 217  $M^{(x+n)^+}$ , one obtains:  
 218

$$\frac{M^{x^+}}{\sum M} = \frac{1}{1 + 10^{(n/4 \log fO_2 + \log K'_{10})}} \quad (14a)$$

219  
 220 and  
 221

$$\frac{M^{(x+n)^+}}{\sum M} = \frac{1}{1 + 10^{-(n/4 \log fO_2 + \log K'_{10})}} \quad (14b)$$

222  
 223

224 From this equation, it can be seen that  $M^{x^+} / \sum M$  takes a sigmoidal form, constrained to vary  
 225 from 0 to 1, with  $\log fO_2$ . The slope is defined by  $n/4$  (i.e. the number of electrons in the redox  
 226 reaction), and the position in  $\log fO_2$  space over which the transition from one valence state to  
 227 the other occurs is determined by  $\log K'_{10}$  (i.e. the simplified equilibrium constant for the  
 228 homogeneous redox reaction). For elements such as U and V, which have three and four  
 229 possible valence states in the melt,  $\sum M \neq M^{x^+} + M^{(x+n)^+}$ ; instead, more complicated  
 230 formulations are required. In the case of Cr, which can occur as  $Cr^{2+}$ ,  $Cr^{3+}$  and  $Cr^{6+}$ , there is  
 231 essentially no coexistence of  $Cr^{2+}$  and  $Cr^{6+}$ , and hence Equations 14a,b are valid approximations.  
 232

233  
 234

235 The above treatment groups all  $M^{x^+}$  together. However, from a melt structural  
 236 viewpoint, it has been argued that  $Fe^{3+}$  and  $Eu^{3+}$  occur both as dissociated cations and in  
 237 complexes such as  $FeO_2^-$  and  $EuO_2^-$  (Fraser, 1975; Ottonello et al., 2001). Although it would be  
 238 possible to write separate reactions for oxidation of  $Fe^{2+}$  to  $Fe^{3+}$  and  $FeO_2^-$ , the resulting  
 239 equations would have an identical mathematical form to the simple model we present here. Our  
 240 activity coefficients, and the use of a modified equilibrium constant  $\log K'_{10}$ , accommodate the  
 241 terms that would be necessary to account for the speciation of the participating ions. The use of  
 242 a more refined structural model may, however, prove advantageous in describing the  
 243 dependence of  $\log K'_{10}$  on melt composition. This is addressed in greater detail in Moretti (this  
 244 volume).  
 245

246  
 247

## 2.2. Heterogeneous equilibria

248  
 249

250 In the mineral (min) phase, the concentration of M will be given by the sum of all  
 251 possible valence states, each with its own partitioning reaction:  
 252

$$M^{x^+}_{\text{mineral}} = [M^{x^+}O_{x/2}]_{\text{melt}} + \sum [N^{x^+}O_{x/2}]_{\text{melt}} \quad (15)$$

253  
 254

253 where  $N^{x+}O_{x/2}$  are the ‘stoichiometric’ control needed to form the phase component in which  
 254  $M^{x+}O_{x/2}$  occurs (O’Neill and Eggins, 2002). The equilibrium constant for this heterogeneous  
 255 reaction is given by:

$$K_{15} = \frac{X_{M^{x+}}^{\min} \gamma_{M^{x+}O}^{\min}}{X_{M^{x+}O_{x/2}}^{\text{melt}} \gamma_{M^{x+}O_{x/2}}^{\text{melt}} \prod a_{N^{x+}O_{x/2}}^{\text{melt}}} \quad (16)$$

257  
 258 where,  $\prod a_{N^{x+}O_{x/2}}$  is the product of the activities of the components  $N^{x+}O_{x/2}$  that make up the  
 259 ‘stoichiometric control’ in the melt. The mineral/melt partition coefficient for each valence state  
 260 of M is given by:

$$D_{M^{x+}} = \frac{\gamma_{M^{x+}O}^{\min}}{K_{15} \left( \gamma_{M^{x+}O_{x/2}}^{\text{melt}} \prod a_{N^{x+}O_{x/2}}^{\text{melt}} c \right)} \quad (17)$$

263  
 264 where  $c$  is a constant to convert mole fractions to concentrations by weight. From this equation,  
 265 it becomes clear that the mineral/melt partitioning of M will depend on the activities of the  
 266 major element oxides in the system, even if they mix ideally.

### 267 2.3. Mineral/melt partitioning as a function of $fO_2$

270 The mineral/melt partition coefficient of a redox-sensitive element M at constant  
 271 pressure, temperature, and major element composition can be defined (alternatively to  
 272 Equation 9) as the sum of the concentrations of all valence states in the mineral phase, divided  
 273 by the sum of the concentration of all valence states in the melt phase:

$$D_M = \frac{\sum [M_{\min}^{x+}]}{\sum [M_{\text{melt}}^{x+}]} \quad (18)$$

274  
 275 Assuming that M occurs in the valence states 1+, 2+, 3+..., this equation can be re-arranged to:

$$D_M = \frac{\frac{[M_{\min}^{1+}]}{[M_{\text{melt}}^{1+}]} + \frac{[M_{\min}^{2+}]}{[M_{\text{melt}}^{1+}]} + \frac{[M_{\min}^{3+}]}{[M_{\text{melt}}^{1+}]} \dots}{1 + \frac{[M_{\text{melt}}^{2+}]}{[M_{\text{melt}}^{1+}]} + \frac{[M_{\text{melt}}^{3+}]}{[M_{\text{melt}}^{1+}]} \dots} \quad (19)$$

281  
 282 Homogeneous redox reactions can be written relating the different valence states to either the  
 283 more reduced or oxidized end-members:



286 ...

287 and the ratios of the concentrations of these related to  $K'$  and  $fO_2$  in the following way:

$$288 \quad [M_{\text{melt}}^{3+}]/[M_{\text{melt}}^{1+}] = (fO_2)^{0.5} K'_{20a} \quad (21a)$$

$$293 \quad [M_{\text{melt}}^{2+}]/[M_{\text{melt}}^{1+}] = (fO_2)^{0.25} K'_{20b} \quad (21b)$$

294 ...

295

296 Substituting Equation 21 into Equation 19 and re-arranging gives:

297

$$D_M = \frac{D^{1+} + [D^{2+}(fO_2)^{0.25}K'_{20b}] + [D^{3+}(fO_2)^{0.5}K'_{20a}] + \dots}{1 + [(fO_2)^{0.25}K'_{20b}] + [(fO_2)^{0.5}K'_{20a}] + \dots} \quad (22)$$

298

299

300 For convenience, this expression can also be written in the following form:

301

$$D_M = \frac{D^{1+} + (D^{2+} 10^{0.25 \log fO_2 + \log K'_{20b}}) + (D^{3+} 10^{0.5 \log fO_2 + \log K'_{20a}}) + \dots}{1 + (10^{0.25 \log fO_2 + \log K'_{20b}}) + (10^{0.5 \log fO_2 + \log K'_{20a}}) + \dots} \quad (23)$$

302

303

304 which then allows for the  $\log fO_2$  term to be substituted more readily by oxygen fugacity terms  
305 relative to buffers in the customary way (e.g.  $\Delta FMQ$ ,  $\Delta IW$ , etc.) as a form of minimizing the effect  
306 of temperature and pressure, if non-isobaric/isothermal data are considered.

307

308

### 309 3. Transition metals (Fe, Cr, Ti, V)

310

311 A large number of transition metals (those elements whose atoms have incompletely  
312 filled  $3d$  orbitals) occur in more than one valence state under magmatic  $fO_2$  conditions (Fig. 2).  
313 Amongst the redox-sensitive first-row transition metals, Fe is a major constituent of the solar  
314 system while others like Ti, V, and Cr occur in minor-to-trace concentrations (Palme and O'Neill,  
315 2014). Mineral/melt partition relations of transition metals are harder to constrain in  
316 comparison with other trace elements as their behavior frequently does not obey Henry's Law.  
317 Furthermore, their electronic configuration results in strong crystal-field effects (Burns, 1993)  
318 and hence partitioning behavior is often anomalous in the context of lattice strain theory.

319

320

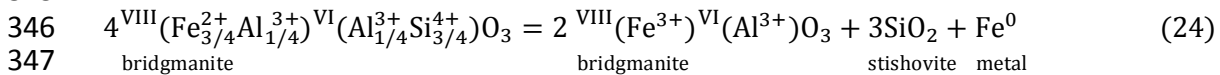
#### 321 3.1. Iron (Fe)

322

323 As the only redox-sensitive cation that is a major element component in the solar  
324 system, iron has a fundamental role in magmatic redox processes. Arguably,  $fO_2$  in the solid  
325 Earth is entirely controlled by the partitioning behavior of iron, which occurs as  $Fe^{3+}$  (ferric  
326 iron),  $Fe^{2+}$  (ferrous iron) as well as  $Fe^0$  (metallic iron). The crystal-chemical controls on Fe  
327 partitioning are essential to understanding  $fO_2$  throughout the Earth's mantle. For example, in  
328 the dominant upper mantle phase olivine ( $Mg_2SiO_4$ ), iron occurs almost exclusively in the  
329 divalent form substituting for Mg in octahedral sites (i.e.  $Fe^{3+}/\Sigma Fe \sim 0$ ; O'Neill et al. 1993). This  
330 means that, in a system closed to oxygen, a reduced basaltic melt that crystallizes olivine will  
331 become oxidized (i.e. its  $Fe^{3+}/\Sigma Fe$  will increase). Conversely, an oxidized melt that crystallizes  
332 magnetite ( $Fe^{2+}Fe_2^{3+}O_4$ , with  $Fe^{3+}/\Sigma Fe \sim 0.66$ ) will become reduced (i.e. its  $Fe^{3+}/\Sigma Fe$  will  
333 decrease). Other ferromagnesian minerals in the upper mantle (e.g. pyroxenes, amphiboles,  
334 garnets) will also contribute to this mass balance.

335

336 Another fundamental example that illustrates the significance of crystal-chemical  
 337 controls on the partitioning behavior of Fe comes from the most abundant mineral phase in the  
 338 Earth's mantle, bridgmanite (Fe,Mg)(Si,Al)O<sub>3</sub>. Bridgmanite can contain up to 20 atomic % Fe, a  
 339 substantial proportion of which is trivalent (Fe<sup>3+</sup>/ΣFe up to 0.6; McCammon, 1997; Frost et al.,  
 340 2004). This preference of bridgmanite for ferric iron occurs because the coupled substitution of  
 341 Fe<sup>3+</sup> on to the VIII-fold coordinated Mg site, charge balanced by Al substitution on to the VI-fold  
 342 coordinated Si site, is energetically favorable (Kesson et al., 1995). Therefore, Fe<sup>3+</sup> occurs in  
 343 experimentally grown Al-bearing bridgmanite even at very reducing conditions, with fO<sub>2</sub>  
 344 maintained low via a disproportionation reaction that form metallic iron (e.g. Shim et al., 2017):



349 These types of disproportionation reactions are powerful in explaining the paradoxical evidence  
 350 suggesting high Fe<sup>3+</sup> contents in the very reduced lower mantle (McCammon, 2005).

351  
 352 In other abundant ferromagnesian minerals such as pyroxenes, the incorporation of  
 353 Fe<sup>2+</sup> and Fe<sup>3+</sup> is also strongly dictated by stoichiometric controls. The experimental data of  
 354 McCanta et al. (2004), for instance, highlight significant steric constraints on the substitution of  
 355 Fe<sup>3+</sup> for Fe<sup>2+</sup> in pigeonite (low Ca clinopyroxene) compared to augite (high Ca clinopyroxene).  
 356 The limited incorporation of Fe<sup>3+</sup> into pigeonite is such that even under highly oxidizing  
 357 conditions only a few percent of the total Fe will be trivalent. In contrast, alkali pyroxenes like  
 358 aegirine (NaFe<sup>3+</sup>Si<sub>2</sub>O<sub>6</sub>) have a strong affinity for Fe<sup>3+</sup> but will not precipitate, even under  
 359 oxidized conditions, unless there is sufficient Na available in the melt. As there is complete solid  
 360 solution between augite and aegirine, Fe<sup>3+</sup>/Fe<sup>2+</sup> of a pyroxene has a complex dependence on  
 361 melt composition when Fe is a major element, and lies beyond the scope of this discussion. A  
 362 related issue arises with the partitioning of trace elements into magnetite, which is strongly fO<sub>2</sub>-  
 363 dependent. However, this is mostly due to the stoichiometric control by the Fe<sup>3+</sup>/Fe<sup>2+</sup> ratio of  
 364 the melt rather than any variation in oxidation state of the trace elements themselves. For  
 365 example, Ti becomes less compatible from FMQ to FMQ+4, well outside the range at which any  
 366 Ti<sup>3+</sup> is present, and this behavior is also exhibited by redox-invariant trace elements such as Zr  
 367 and Hf (Siewwright et al., 2017). Hence, care should be taken when evaluating redox-related  
 368 trends in Fe-rich systems to understand the factors contributing to variations in partition  
 369 coefficients. The relationships described in this chapter are only applicable to trace components  
 370 of melts and minerals.

371  
 372 Based on experiments with simplified synthetic compositions doped with small  
 373 concentrations of Fe as a function of fO<sub>2</sub>, Mallmann and O'Neill (2009) showed that  $D_{\text{Fe}^{2+}} \gg$   
 374  $D_{\text{Fe}^{3+}}$  in olivine and orthopyroxene, but  $D_{\text{Fe}^{2+}} < D_{\text{Fe}^{3+}}$  in clinopyroxene and spinel (Fig. 3a).  
 375 Amphibole/melt data from King et al. (2000) indicates that the partitioning of both Fe<sup>3+</sup> and  
 376 Fe<sup>2+</sup> are both close to unity, with  $D_{\text{Fe}^{3+}}$  about a factor of two higher than  $D_{\text{Fe}^{2+}}$  (though the range  
 377 of fO<sub>2</sub> in this study, from FMQ-6 to FMQ+3, is not sufficient to constrain either Fe<sup>2+</sup> or Fe<sup>3+</sup>, so  
 378 the differences in  $D$ s between the two species are likely larger). The data of Martel et al. (1999)  
 379 and Krawczynski et al. (2012), which examined fO<sub>2</sub> over an even more limited range alongside  
 380 the effects of H<sub>2</sub>O,  $T$  and  $P$ , show higher  $D_{\text{Fe}}/D_{\text{Mg}}$  at more oxidizing conditions, supporting a  
 381 higher compatibility for Fe<sup>3+</sup> in igneous amphiboles. It should be noted in passing that  
 382 amphibole Fe<sup>3+</sup>/ΣFe is readily altered by a redox reaction  $\text{Fe}^{2+} + \text{OH}^- = \text{Fe}^{3+} + \text{O}^{2-} + \frac{1}{2} \text{H}_2$ , and  
 383 hence may not preserve magmatic values (Popp et al., 1995).

384  
 385 In non-ferromagnesian minerals such as feldspars, iron behaves as a typical trace  
 386 element. In plagioclase feldspar for instance (Fig. 3a), Fe<sup>3+</sup> ( $r^{\text{IV}} = 0.49 \text{ \AA}$ )<sup>1</sup> is significantly more

<sup>1</sup> Ionic radii reported in this study were taken from Shannon (1976).

387 compatible than  $\text{Fe}^{2+}$  (Phinney, 1992; Wilke and Behrens, 1999) as it directly substitutes for  
 388  $\text{Al}^{3+}$  ( $r^{\text{IV}} = 0.39 \text{ \AA}$ ) in tetrahedral sites, as opposed to  $\text{Fe}^{2+}$  which is significantly smaller ( $r^{\text{VIII}} =$   
 389  $0.78 \text{ \AA}$ ) than the larger VIII-fold coordinated A-site ( $r_0 \sim 1.2 \text{ \AA}$ ) (Longhi et al., 1976). In some  
 390 oxidized peralkaline lavas, alkali feldspars with up to 2.8 wt.%  $\text{Fe}_2\text{O}_3$  have been reported (Mann  
 391 et al. 2006). Lundgaard and Tegner (2004) found a strong dependence of  $D_{\text{Fe}^{2+}}$  and  $D_{\text{Fe}^{3+}}$  on melt  
 392 composition, particularly  $\text{SiO}_2$ , but not on plagioclase composition.  
 393  
 394

### 395 3.2. Chromium (Cr)

396  
 397 Chromium can exist as  $\text{Cr}^{2+}$ ,  $\text{Cr}^{3+}$  and  $\text{Cr}^{6+}$  in magmas (e.g. Berry and O'Neill, 2004;  
 398 Schreiber and Haskin, 1976), but direct detection of  $\text{Cr}^{2+}$  in quenched basaltic melts is hindered  
 399 by an electron exchange with Fe on quenching (Reaction 1; Berry et al., 2003). Mineral-melt  
 400 partitioning relations, however, have long indicated the presence of  $\text{Cr}^{2+}$  in silicate melts over  
 401 typical magmatic conditions (e.g. Barnes, 1986; Hanson and Jones, 1998; Postovetov and  
 402 Roeder, 2000). The divalent and trivalent species of Cr overwhelmingly dominate over typical  
 403 magmatic  $f\text{O}_2$ s (Fig. 2), with hexavalent Cr only becoming stable at very oxidizing conditions  
 404 (usually  $> \text{FMQ}+4$ ; Berry and O'Neill, 2004). Because such highly oxidizing conditions are  
 405 uncommon in magmatic systems, and  $\text{Cr}^{6+}$  appears to be highly incompatible in high-  
 406 temperature mineral phases (Mallmann and O'Neill, 2009), the presence of small amounts of  
 407  $\text{Cr}^{6+}$  in magmas should have no significant effect on the bulk partitioning of Cr (although it  
 408 should be noted that the transition from  $\text{Cr}^{3+}$  to  $\text{Cr}^{6+}$  is expected to occur over a relatively  
 409 narrow range of  $f\text{O}_2$  given that the redox reaction involves three electrons). High-temperature  
 410 experiments under the highly oxidizing conditions necessary to constrain the behavior of  $\text{Cr}^{6+}$   
 411 are limited (hexavalent Cr appears to be volatile at high temperature; Wijbrans et al., 2015), so  
 412 the focus of our discussion will be on  $\text{Cr}^{2+}$  and  $\text{Cr}^{3+}$ .  
 413

414 Chromium is a major constituent of many rock-forming minerals (Burns and Burns,  
 415 1975), normally making end-member components where  $\text{Cr}^{3+}$  substitutes for  $\text{Al}^{3+}$  (and  $\text{Fe}^{3+}$ ).  
 416 Some of these substitutions are complete solid solutions, most notably between spinel  
 417 ( $\text{MgAl}_2^{3+}\text{O}_4$ ) and magnesiochromite ( $\text{MgCr}_2^{3+}\text{O}_4$ ), and between grossular ( $\text{Ca}_3\text{Al}_2^{3+}\text{Si}_3\text{O}_{12}$ ) and  
 418 uvarovite ( $\text{Ca}_3\text{Cr}_2^{3+}\text{Si}_3\text{O}_{12}$ ). In most cases,  $\text{Cr}^{3+}$  only occurs in octahedral coordination, as a  
 419 result of its large crystal-field stabilization energy (CFSE; Burns, 1993). The ionic radius of  $\text{Cr}^{3+}$   
 420 is also significantly larger than  $\text{Al}^{3+}$  (and hence  $\text{Si}^{4+}$ ), making it difficult for tetrahedral  
 421 substitution. Incorporation of  $\text{Cr}^{2+}$  is unfavored due to its electronic configuration, which in  
 422 octahedral coordination induces a destabilizing crystal-field energy and Jahn-teller distortions  
 423 (Burns, 1975). Hence,  $\text{Cr}^{2+}$  can substitute for  $\text{Mg}^{2+}$  but only to a limited extent, and endmember  
 424  $\text{Cr}^{2+}$  silicates do not occur in nature (Li et al., 1995).  
 425

426 The importance of Cr to mantle phase equilibria (e.g. Liu and O'Neill, 2004), the link  
 427 between chromite and precious metals (e.g. platinum group elements, PGE) in layered  
 428 intrusions (e.g. Barnes, 1986), and its utility as an oxybarometer in magmatic systems (e.g.  
 429 Postovetov and Roeder, 2000) has prompted numerous studies aimed at determining Cr  
 430 solubility in silicate melts (e.g. Roeder and Reynolds, 1991) and its partitioning between  
 431 associated phases. Here we focus on minerals where Cr substitutes as a trace component, as this  
 432 allows us to constrain the effect of  $f\text{O}_2$  on the partitioning behavior of both  $\text{Cr}^{2+}$  and  $\text{Cr}^{3+}$ .  
 433

434 Amongst minerals where Cr substitutes as trace element, olivine has the largest  
 435 available experimental partitioning dataset as a function of  $f\text{O}_2$ . In olivine,  $\text{Cr}^{2+}$  ( $r^{\text{VI}} = 0.80 \text{ \AA}$ ) is  
 436 incorporated by direct replacement of  $\text{Mg}^{2+}$  ( $r^{\text{VI}} = 0.72 \text{ \AA}$ ) in octahedral sites without significant  
 437 lattice distortion (Reaction 5; Jollands et al., 2018). Substitution of  $\text{Cr}^{3+}$  ( $r^{\text{VI}} = 0.615 \text{ \AA}$ ) into  
 438 olivine octahedral sites, on the other hand, creates charge imbalance that can be accounted for  
 439 either by octahedral vacancies (Reaction 6; Hanson and Jones, 1998; Jollands et al., 2018; Papike

440 et al., 2005), or by coupled substitution with  $\text{Al}^{3+}$  and  $\text{Si}^{4+}$  in tetrahedral sites (Reaction 7;  
441 Jollands et al., 2018).

442

443 Olivine/melt partitioning studies from Schreiber and Haskin (1976) and Hanson and  
444 Jones (1998) in the  $\text{CaO-MgO-Al}_2\text{O}_3\text{-SiO}_2$  (CMAS) show a systematic dependence of  $D_{\text{Cr}^{3+}}$  on melt  
445 composition (Fig. 4), though the dependence is not straightforward, suggesting that both  
446 substitution mechanisms described above likely operate. Hanson and Jones (1998), however,  
447 were able to parameterize  $D_{\text{Cr}^{3+}}$  between olivine and melt using the universal melt descriptor  
448  $\text{NBO}/T$  ( $D_{\text{Cr}^{3+}} = -0.39 \text{NBO}/T + 1.29$ ). For  $\text{Cr}^{2+}$ , however, partitioning between olivine and melt  
449 appears to be independent of melt composition, but varies slightly with temperature (Hanson  
450 and Jones, 1998). More often than not,  $D_{\text{Cr}^{2+}}$  is nearly equal to  $D_{\text{Cr}^{3+}}$  between olivine and melt  
451 (including for basaltic compositions), so that effectively no change in bulk Cr partitioning is  
452 detected as a function of  $f\text{O}_2$  (Mallmann and O'Neill, 2009; Hanson and Jones, 1998; Fig. 3b).  
453 Direct Cr valence measurements in olivine by XANES have confirmed these findings (Bell et al.  
454 2014).

455

456 Mallmann and O'Neill (2009) found that  $\text{Cr}^{2+}$  is similarly partitioned amongst olivine,  
457 ortho- and clinopyroxene, but  $\text{Cr}^{3+}$  is significantly more compatible in pyroxenes, particularly  
458 clinopyroxene (Fig. 3b). This is not surprising given that  $\text{Cr}^{3+}$  ( $r^{\text{VI}} = 0.615 \text{ \AA}$ ) has an ionic radius  
459 that is similar to the ideal strain-free octahedral M1 site of clinopyroxenes for trivalent cations  
460 ( $r_0^{3+, \text{M1}} \sim 0.668 \text{ \AA}$ ; Hill et al., 2000).  $\text{Cr}^{2+}$  ( $r^{\text{VI}} = 0.80 \text{ \AA}$ ), on the other hand, is significantly larger  
461 than the ideal M1 site of clinopyroxenes for divalent cations ( $r_0^{2+, \text{M1}} \sim 0.69 \text{ \AA}$ ; Hill et al., 2000).  
462 Mallmann and O'Neill (2009) noted a significant difference between the partitioning of  $\text{Cr}^{3+}$   
463 between clinopyroxene and melt obtained for their compositions V1 and V7 (which are  
464 identical except for the Cr-doping levels), suggesting that  $\text{Cr}^{3+}$  does not behave according to  
465 Henry's Law in the concentration range of these experiments ( $> 1.5 \text{ wt.}\%$   $\text{Cr}_2\text{O}_3$ ), probably  
466 because of the strong coupling of  $\text{Cr}^{3+}$  with  $\text{Al}^{3+}$  in pyroxenes (Klemme and O'Neill, 2000).  
467 Chromium is noticeably more compatible in augite compared to pigeonite and enstatite, given  
468 the availability of cations ( $\text{Al}^{3+}$  and  $\text{Na}^+$ ) for charge balancing the substitution of  $\text{Cr}^{3+}$  for Mg in  
469 octahedral sites (Karner et al., 2007; Mallmann and O'Neill, 2009). Interestingly,  $\text{Cr}^{2+}$  appears to  
470 be dominant species entering the structure of lower mantle phases such as ferropericlase and  
471 bridgmanite (Eeckhout et al., 2007). Neither  $\text{Cr}^{3+}$  nor  $\text{Cr}^{2+}$  appears to be easily incorporated  
472 into plagioclase (Aigner-Torres et al., 2007) as  $\text{Cr}^{3+}$  is too large for the tetrahedral site, and  $\text{Cr}^{2+}$   
473 too small for the large distorted VIII-fold coordinated site.

474

475 Finally, we note that Cr is a well-known outlier in lattice-strain parabolas due to large  
476 crystal-field effects, so the prediction of  $\text{Cr}^{2+}$  and  $\text{Cr}^{3+}$  partitioning using lattice strain models  
477 should be done with great caution.

478

479

### 480 3.3. Titanium (Ti)

481

482 Titanium primarily occurs as  $\text{Ti}^{4+}$  over most of the range of  $f\text{O}_2$ s relevant to planetary  
483 scientists, but spectroscopic studies indicate that under very reducing conditions (i.e. below  
484 FMQ-4) a substantial fraction of Ti occurs as  $\text{Ti}^{3+}$  (Schreiber, 1977). The transition from  $\text{Ti}^{3+}$  to  
485  $\text{Ti}^{4+}$  appears to be strongly dependent on melt composition (Borisov, 2012; Fig. 2). Hence,  
486 although the partitioning of Ti is a poor oxybarometer for terrestrial magmatism, it is markedly  
487 more relevant to understanding the geochemical evolution of the early solar nebula and  
488 reduced bodies such as the Moon (Fig. 2).

489

490 Hibonite ( $\text{CaAl}_{12}\text{O}_{19}$ ) occurs in the calcium aluminum-rich inclusions (CAIs) of  
491 chondritic meteorites. It is one of the earliest phases to condense from the solar nebula, and can  
492 contain up to 8 wt%  $\text{TiO}_2$  (Allen et al., 1978). The blue color of many hibonite grains has been  
493 shown to be due to the presence of  $\text{Ti}^{3+}$  (Burns and Burns, 1984; Sutton et al., 2017),

494 incorporated as a  $\text{CaTi}_2^{3+}\text{Al}_{10}\text{O}_{19}$  component, but  $\text{Ti}^{4+}$  can also be accommodated in hibonite via  
 495 a coupled substitution with Mg, as a  $\text{CaMg}_2\text{Ti}_2^{4+}\text{Al}_8\text{O}_{19}$  component (Doyle et al., 2014). The  
 496 coupled nature of the substitution of  $\text{Ti}^{4+}$  means that the availability of Mg exerts a strong  
 497 control on  $\text{Ti}^{3+}/\Sigma\text{Ti}$  (where  $\Sigma\text{Ti} = \text{Ti}^{3+} + \text{Ti}^{4+}$ ) in hibonite; since it is often unclear which phases  
 498 are in equilibrium in CAIs, this oxybarometer may have limited utility (Berry et al., 2017).  
 499

500  $\text{Ti}^{3+}$  is more compatible than  $\text{Ti}^{4+}$  in the majority of phases, including olivine, diopside,  
 501 orthopyroxene and anorthite (Mallmann and O'Neill, 2009; Peters et al., 1995; Fig. 3c). Ti K-  
 502 edge XANES measurements of both synthetic and natural lunar basalt samples have revealed  
 503 that  $\text{Ti}^{3+}$  is enriched in ilmenite, armalcolite and clinopyroxene at  $f\text{O}_2$  of about FMQ-4.5 (Leitzke  
 504 et al., 2018; Simon and Sutton, 2018). However, as it is most compatible in clinopyroxene,  
 505 essentially all research has focused on this phase. Indeed, a  $\text{Ti}^{3+}$ -pyroxene (grossmanite,  
 506  $\text{CaTi}^{3+}\text{AlSiO}_6$ ) has been reported from the Allende meteorite, and  $\text{NaTi}^{3+}\text{Si}_2\text{O}_6$  has been  
 507 synthesized experimentally (Ohashi et al., 1982; Ma and Rossman, 2009). Although quantitative  
 508 oxybarometry is hampered by multiple sources of uncertainty, including the equilibrium  
 509 mineral assemblage (as with hibonite), the mixing relations of Ti-bearing pyroxenes and the  
 510 temperature of formation, decreasing  $\text{Ti}^{3+}/\Sigma\text{Ti}$  from core to rim of some CAIs suggests  
 511 increasingly oxidizing conditions in the solar nebula over a period of up to 300 kyr, perhaps by  
 512 as much as 6 – 7 log  $f\text{O}_2$  units (Young et al., 2012). However, in some CAIs an oxidation trend,  
 513 followed by a more reduced rim, has been observed. This is attributed to incompatible  $\text{Ti}^{4+}$   
 514 concentrating in the melt phase, which was isolated from the solar nebula by a thick melilite  
 515 mantle, followed by late-stage ingress of nebular gases to reduce the residual melt prior to  
 516 crystallization of the rims (Papike et al., 2016).  $\text{Ti}^{3+}$  has also been observed in lunar pyroxenes  
 517 (Burns et al., 1972), but is thought to be a minor component even on such a reduced planetary  
 518 body (Papike et al., 2005). Terrestrial magmas generally form at far more oxidizing conditions  
 519 and Ti is expected to occur exclusively as  $\text{Ti}^{4+}$  (Fig. 2). Pyroxenes in the native iron-bearing  
 520 lavas of Disko Island, Greenland, have been suggested to contain some  $\text{Ti}^{3+}$  (Pedersen, 1981),  
 521 but this is speculative and may not be compatible with the rather high Fe contents.  
 522

523

### 524 3.4. Vanadium (V)

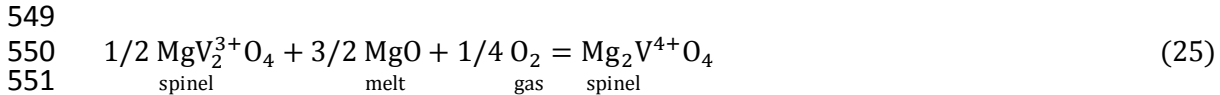
525

526 Vanadium is the redox-sensitive trace element that occurs in the largest number of  
 527 valence states at typical magmatic  $f\text{O}_2$ s (Fig. 2), namely  $\text{V}^{2+}$ ,  $\text{V}^{3+}$ ,  $\text{V}^{4+}$  and  $\text{V}^{5+}$  (Borisov et al.,  
 528 1987; Schreiber et al., 1987; Sutton et al., 2005). Given the plethora of valence states with  
 529 theoretically contrasting geochemical behaviors, significant effort has been made to  
 530 characterize the effect of  $f\text{O}_2$  and other variables such as pressure, temperature, mineral and  
 531 melt composition on the partitioning of V in silicate/oxide phases relevant to mantle melting  
 532 and magmatic differentiation (e.g. Arató and Audétat, 2017; Canil 1997; 1999; 2002; Canil and  
 533 Fedortchouk, 2000; 2001; Karner et al., 2008; Laubier et al., 2014; Mallmann and O'Neill, 2009;  
 534 2013; Papike et al., 2015; Righter et al. 2006a,b; 2011; Shearer et al., 2006; Sievwright et al.,  
 535 2017; Toplis and Corgne 2002; Wijbrans et al., 2015). The end goal of many of these studies is to  
 536 calibrate the sensitivity of V partitioning to  $f\text{O}_2$  as an oxybarometer.  
 537

538

539 Under terrestrial magmatic  $f\text{O}_2$  conditions (Fig. 2),  $\text{V}^{3+}$  and  $\text{V}^{4+}$  are the dominant valence  
 540 states, and spinel the major mineral group host. In pure magnetite ( $\text{Fe}^{2+}\text{Fe}_2^{3+}\text{O}_4$ ), where the  
 541 stoichiometry fixes  $\text{Fe}^{3+}/\text{Fe}^{2+}$  at 2, incorporation of vanadium occurs via an  $f\text{O}_2$ -independent  
 542 electron-exchange reaction:  $\text{Fe}^{3+} + \text{V}^{3+} = \text{Fe}^{2+} + \text{V}^{4+}$  (O'Neill and Navrotsky, 1984). However,  
 543 experimental studies of spinel group minerals have invariably shown strong dependence of  
 544 vanadium partitioning with  $f\text{O}_2$  both in Fe-free and Fe-bearing systems (e.g. Arató and Audétat,  
 545 2017; Canil et al., 1999; Mallmann and O'Neill, 2009; Papike et al., 2015; Righter et al., 2006b;  
 546 Sievwright et al., 2017; Toplis and Corgne, 2002). Importantly, because Fe is an essential  
 component of magnetite, the partitioning of non-redox variable elements depends on  $f\text{O}_2$

547 (Siewwright et al., 2017); this is not the case for Fe-poor spinels. For example, the ratio  $V^{3+}/V^{4+}$   
 548 of pure spinel ( $MgAl_2O_4$ ) is controlled by the reaction:



551  
 552  
 553 It is therefore unsurprising that the bulk partitioning of V between spinel group minerals and  
 554 silicate melt is a strong function of  $fO_2$  as well as composition (mineral and melt). Experimental  
 555 data shows that  $D_{V^{3+}} \gg D_{V^{4+}} > D_{V^{5+}}$  between spinel and silicate melt (Fig. 3d), and that the bulk  
 556 partitioning of vanadium for Cr-spinels is higher than that for Al-spinels (Canil, 2002; Mallmann  
 557 and O'Neill, 2009). The negative correlation between Al and  $V^{3+}$  in experimentally grown  
 558 spinels provides strong evidence that the preferred mode of vanadium substitution into spinel  
 559 is by direct replacement of Al in octahedral sites (Balan et al., 2006; Canil, 2002; Righter et al.,  
 560 2006b). However, the details of the various possible substitution mechanisms are complex,  
 561 given the structure of spinels and the multivalent nature of their cations (e.g. Papike et al.,  
 562 2015). Melt composition also appears to play a significant role, as demonstrated by V  
 563 partitioning experiments between magnetite and silicic melts (Arató and Audétat, 2017).

564  
 565 Owing to its high charge and small ionic radius,  $V^{5+}$  is highly incompatible in all rock-  
 566 forming minerals. When sufficiently oxidized conditions are achieved, the partitioning of  $V^{5+}$   
 567 can be obtained, though this value is typically  $\ll 0.01$  (e.g. Mallmann and O'Neill, 2009).  $V^{4+}$   
 568 has partition coefficients that fall between  $V^{3+}$  and  $V^{5+}$  (Fig. 3d) and therefore is much harder to  
 569 constrain. The ionic radius of  $V^{4+}$  is similar to that of  $Ti^{4+}$  in both octahedral and tetrahedral  
 570 coordination ( $r^{VI} = 0.58$  and  $0.605$  Å;  $r^{IV} = 0.46$  and  $0.42$  Å; for  $V^{4+}$  and  $Ti^{4+}$  respectively), and  
 571 both have similar electronic configurations and thus no significant difference in CFSE, so an  
 572 approximation can be obtained using lattice strain theory. In connection with that, we note that  
 573  $D_{V^{4+}}$  for pyroxene and olivine obtained by Mallmann and O'Neill (2009) are about an order of  
 574 magnitude higher than what is inferred from lattice strain parabolas of other tetravalent  
 575 cations. For some minerals, constraining the partitioning of  $V^{3+}$  may also be difficult when it  
 576 shows compatibility between  $V^{2+}$  and  $V^{4+}$  (e.g. olivine or orthopyroxene). For clinopyroxene  
 577 though,  $V^{3+}$  is clearly more compatible than both  $V^{2+}$  and  $V^{4+}$ , and its partitioning readily  
 578 determined (Fig. 3d). Partition coefficients for  $V^{2+}$  can be obtained if sufficiently reduced  
 579 experimental data is available, such as those reported by Mallmann and O'Neill (2009), but  
 580 extrapolation from lattice strain parabolas should be avoided since  $V^{2+}$  has the same electronic  
 581 configuration as  $Cr^{3+}$  and therefore large CFSE in octahedral coordination (Burns, 1993).

582  
 583 For mineral phases that only crystallize at high pressure from natural magmas,  
 584 partitioning relations are harder to constrain as a function of  $fO_2$  since this intensive parameter  
 585 needs to be buffered externally using double-capsule techniques or internally using low-  
 586 solubility solid metal-oxide. Righter et al. (2011) extended the  $fO_2$  conditions obtained by  
 587 Mallmann and O'Neill (2007, 2009) to constrain the  $D_{V^{3+}}$  in garnet at  $\sim 10$ . The compatibility  
 588 order of vanadium valences in garnet is  $D_{V^{3+}} \gg D_{V^{4+}} > D_{V^{5+}}$ , with values comparable to  
 589 clinopyroxene (Mallmann and O'Neill, 2009). XANES studies by Righter et al. (2011), however,  
 590 suggest that small amounts of  $V^{2+}$  are incorporated into garnet, even under relatively oxidizing  
 591 conditions.

592  
 593 Because of the complexities in developing a thermodynamic partitioning model that  
 594 involves four different oxidation states, all of which likely varying differently with  
 595 compositional parameters, Mallmann and O'Neill (2013) developed an empirical calibration of  
 596 V partitioning between olivine and melt over a restricted range of  $fO_2$ s (from FMQ-4 to FMQ+4),  
 597 where  $\log D_V$  vary more or less linearly with  $\log fO_2$ , accounting for the effects of olivine and  
 598 melt composition. Similarly, Arató and Audétat (2017) developed an empirical calibration for  
 599 magnetite. It would be useful to develop similar models for other common magmatic minerals,  
 600 but this requires more extensive experimental databases since substitution of different V

601 valence states in minerals like pyroxene and garnet are more complex than in olivine and  
602 magnetite.

603

604

#### 605 4. Rare earths (Ce and Eu)

606

607 The rare earth elements (REE), including Y, have favorable characteristics for examining  
608 redox processes. Apart from Ce and Eu, the REE exist exclusively in the trivalent state and their  
609 ionic radii vary smoothly from La to Lu (with Y somewhere between Ho and Er). This provides  
610 excellent coverage for fitting a lattice strain parabola to the REE<sup>3+</sup>; anomalies relative to this  
611 parabola are readily quantifiable, and often visually striking. Zircon is notable because its REE  
612 patterns commonly feature both Ce and Eu anomalies (Fig. 5). They are typically quantified as  
613 Ce/Ce\* and Eu/Eu\*, where Ce\* and Eu\* are the values that would be predicted by interpolation  
614 or extrapolation. The simplest is the geometric mean of La and Pr (i.e., a linear interpolation on  
615 a logarithmic axis):

616

$$617 \text{Ce}^* = (\text{La}_N \times \text{Pr}_N)^{0.5} \quad (26)$$

618

619 where 'N' denotes normalization to CI chondrite, whole rock or matrix glass. La is often below  
620 the limit of detection for analyses of zircon, and so extrapolation from Pr-Nd-Sm may be used  
621 instead. Alternatively, polynomial fits to the REE pattern may be used (e.g. O'Neill, 2016;  
622 Burnham and Berry, 2017). There are systematic deviations between the methods, so values  
623 taken from different sources may need recalculation before being compared.

624

625 Cerium exists as both Ce<sup>3+</sup> and Ce<sup>4+</sup> in magmas. However, at typical magmatic fO<sub>2</sub> the  
626 proportion of Ce<sup>4+</sup> is small (Fig. 2), with Ce<sup>4+</sup>/ΣCe ~ 0.001 (Burnham and Berry, 2012; 2014).  
627 At such low levels, it can be seen from Fig. 6a that where Ce<sup>4+</sup> is less compatible than Ce<sup>3+</sup> there  
628 is no perceptible effect on the bulk partitioning of Ce: even in the most extreme case, i.e.  $D_{\text{Ce}^{4+}} =$   
629  $0$ ,  $D_{\text{Ce}}$  would drop by 0.1 %, an amount that is far less than the achievable analytical accuracy. By  
630 a similar line of logic, it can be calculated that in order for a mineral in a terrestrial magma to  
631 develop a noticeable Ce anomaly, e.g. Ce/Ce\* = 1.1,  $D_{\text{Ce}^{4+}}$  must be greater than  $D_{\text{Ce}^{3+}}$  by a factor of  
632 100. For minerals with a steep or strongly curved REE patterns, or larger analytical  
633 uncertainties, even a 10 % excess of Ce might not be a convincing anomaly.

634

635 Few minerals have a strong affinity for Ce<sup>4+</sup>. The most notable, zircon, will be addressed  
636 in detail below. This is a favorable substitution on account of the identical 4+ charge of Zr, and a  
637 similarly large ionic radius ( $r^{\text{VIII}} = 0.84$  and  $0.97$  Å for Zr and Ce<sup>4+</sup> respectively). Positive Ce  
638 anomalies have been reported from other Zr minerals such as baddeleyite (Schärer et al., 2011),  
639 wadeite (Jaques, 2016), elpidite and armstrongite (Gerdes et al., 2017). Thomson et al. (2016)  
640 reported both positive and negative Ce anomalies for inclusions in diamonds, but the precise  
641 interpretation of these grains is complicated by their polymineralic nature and a lack of  
642 experimental partitioning data.

643

644 Zircon is the commonest of these, and has attracted the most experimental work  
645 (Burnham and Berry, 2012; Trail et al., 2011; 2012). The most recent calibration of the Ce-in-  
646 zircon oxybarometer uses lattice strain theory to infer  $D_{\text{Ce}^{3+}}$  and  $D_{\text{Ce}^{4+}}$ , which allow Ce<sup>4+</sup>/ΣCe in  
647 the melt to be calculated and the corresponding fO<sub>2</sub> deduced (Smythe and Brenan, 2016). This  
648 approach avoids the challenge of growing analyzable well-equilibrated zircon crystals, but there  
649 is presently a discrepancy between the two available models for Ce speciation in silicate melts  
650 (Burnham and Berry, 2014; Smythe and Brenan, 2015) and hence further work is required to  
651 develop a robust version of this oxybarometer.

652

653 For other minerals, there has been no systematic study of the effect of fO<sub>2</sub>, but this can  
654 be predicted by a combination of lattice strain modelling (and for minerals with more than one

655 cation site, whose 4+ parabolas are underconstrained, by making the approximation  $D_{\text{Ce}^{4+}} =$   
 656  $D_{\text{U}^{4+}}$  and  $\text{Ce}^{4+}/\Sigma\text{Ce}$  estimated from the optical basicity of the melt composition (Burnham and  
 657 Berry, 2014). It can be seen that  $\text{Ce}^{4+}$  is less compatible than  $\text{Ce}^{3+}$  in Zr-free minerals and that,  
 658 as explained above,  $D_{\text{Ce}}$  does not change appreciably in the  $f\text{O}_2$  range of natural magmas.  
 659

660 Although the foregoing discussion considered mineral/melt partitioning, it is not always  
 661 possible to consider mineral compositions in terms of mineral/melt partition coefficients. In  
 662 particular, plutonic rocks do not retain any melt fraction, but even volcanic rocks often contain a  
 663 significant cargo of crystals that are substantially older and may not be in equilibrium with their  
 664 present host (e.g. Murphy et al., 1998). In the case of Ce, it is possible to use the bulk rock or  
 665 even CI chondrite as a normalization factor, because magma compositions with Ce anomalies  
 666 are uncommon. It is often stated that subduction zone magmas can have  $\text{Ce}/\text{Ce}^* < 1$ , indicating  
 667 the incorporation of Ce-depleted sediments. As highlighted by O'Neill (2016), however, many  
 668 reported examples of Ce anomalies in lavas are poorly constrained. Relatively small negative Ce  
 669 anomalies,  $\text{Ce}/\text{Ce}^* \sim 0.9$ , are known in a variety of subduction settings (e.g. Hastie et al., 2009;  
 670 Woodhead, 1989). As zircon Ce anomalies are typically one or two orders of magnitude larger,  
 671 failure to account for a pre-existing Ce anomaly in the magma results in an underestimate of log  
 672  $f\text{O}_2$  of  $< 0.2$ . The same is not true for Eu.  
 673

674 Europium can exist as  $\text{Eu}^{2+}$  and  $\text{Eu}^{3+}$  in magmas. The transition occurs most rapidly  
 675 below the FMQ buffer, a range over which  $\text{Fe}^{3+}/\Sigma\text{Fe}$  changes more slowly, and hence it is  
 676 potentially a useful oxybarometer for reduced magmas (Fig. 2). The crystal chemistry of  $\text{Eu}^{2+}$   
 677 ( $r^{\text{VI}} = 1.17 \text{ \AA}$ ) can be thought of as similar to  $\text{Sr}^{2+}$  ( $r^{\text{VI}} = 1.18 \text{ \AA}$ ), and indeed there is even a  $\text{Eu}^{2+}$   
 678 feldspar (Kimata, 1988). In contrast,  $\text{Eu}^{3+}$  behaves as a typical middle REE. Accordingly,  $D_{\text{Eu}^{2+}} >$   
 679  $D_{\text{Eu}^{3+}}$  for plagioclase and alkali feldspars and åkermanitic melilite (Kuehner et al., 1989), but for  
 680 most other minerals  $D_{\text{Eu}^{3+}} > D_{\text{Eu}^{2+}}$  (Fig. 6b). Plagioclase feldspar and clinopyroxene are by far the  
 681 most-studied in terms of Eu partitioning as a function of  $f\text{O}_2$  and the following discussion will be  
 682 restricted to these, although phases such as titanite, with  $D_{\text{Eu}^{3+}}/D_{\text{Eu}^{2+}} \approx 2500$  may be important  
 683 to consider for some igneous systems (Loader et al., 2017).  
 684

685 There are various models that allow plagioclase/melt  $D_{\text{Eu}^{2+}}$  and  $D_{\text{Eu}^{3+}}$  to be predicted  
 686 using lattice strain theory (Aigner-Torres et al., 2007; Dohmen and Blundy, 2014).  
 687 Corresponding models for clinopyroxene and other minerals have not been developed, and even  
 688 in the case of plagioclase, Eu oxybarometry will be more precise where measured values of  
 689 partition coefficients for proxy elements are used for  $D_{\text{Eu}^{2+}}$  and  $D_{\text{Eu}^{3+}}$ . Rearranging Equation 9, we  
 690 can approximate  $\text{Eu}^{3+}/\Sigma\text{Eu}$  by:  
 691

$$692 \text{Eu}^{3+}/\Sigma\text{Eu} = (D_{\text{Eu}} - D_{\text{Sr}})/(D_{\text{MREE}} - D_{\text{Sr}}) \quad (27)$$

693  
 694 where  $D_{\text{Eu}}$  is the observed Eu partition coefficient and  $D_{\text{MREE}}$  is an estimate of  $D_{\text{Eu}^{3+}}$ , i.e.  $D_{\text{Sm}}$ ,  $D_{\text{Gd}}$ ,  
 695 or preferably  $(D_{\text{Sm}} \times D_{\text{Gd}})^{0.5}$ . For values of  $\text{Eu}^{3+}/\Sigma\text{Eu}$  in the range 0.1 to 0.9, the  $f\text{O}_2$  can be  
 696 calculated by rearranging the general equation from Burnham et al. (2015):  
 697

$$698 \log f\text{O}_2 = 40.4 - 25640/T - 56.8\Lambda - 4 \log (\Sigma\text{Eu}/\text{Eu}^{3+} - 1) \quad (28)$$

699  
 700 where  $T$  is temperature in Kelvin, and  $\Lambda$  is optical basicity, which can be calculated as:  
 701

$$702 \Lambda = \frac{\frac{\text{SiO}_2}{62.6} + \frac{\text{TiO}_2}{36.3} + \frac{\text{Al}_2\text{O}_3}{56.6} + \frac{\text{FeO}}{55.8} + \frac{\text{MgO}}{51.7} + \frac{\text{CaO}}{56.1} + \frac{\text{Na}_2\text{O}}{53.2} + \frac{\text{K}_2\text{O}}{67.3}}{\frac{\text{SiO}_2}{30.04} + \frac{\text{TiO}_2}{39.9} + \frac{\text{Al}_2\text{O}_3}{34} + \frac{\text{FeO}}{55.8} + \frac{\text{MgO}}{40.3} + \frac{\text{CaO}}{56.1} + \frac{\text{Na}_2\text{O}}{62} + \frac{\text{K}_2\text{O}}{94.2}} \quad (29)$$

704 with all oxide components in wt. %, and no distinction drawn between  $\text{Fe}^{2+}$  and  $\text{Fe}^{3+}$ . The effect  
 705 of  $\text{H}_2\text{O}$  was not included in the optical basicity model of Duffy (1993) and hence is not  
 706 considered here. At natural concentrations,  $\text{MnO}$  and  $\text{P}_2\text{O}_5$  have negligible influence (e.g. 0.5  
 707 wt.%  $\text{P}_2\text{O}_5$  would change  $\log K'$  for  $\text{Eu}^{2+}$ - $\text{Eu}^{3+}$  by  $\sim 0.02$ ).

708

709 With values of  $\text{Eu}^{3+}/\Sigma\text{Eu}$  outside the range 0.1 to 0.9, the reliability of this type of  
 710 oxybarometer is compromised by the shallow slope of  $M^{x+}/\Sigma M$  against  $f\text{O}_2$ . An error of  $\pm 0.03$   
 711 propagates to more than a log unit of  $f\text{O}_2$ . A key challenge in using Eu partitioning to determine  
 712  $f\text{O}_2$  is the strong dependence of  $\log K'$  on melt composition (Aigner-Torres et al., 2007; Burnham  
 713 and Berry, 2015). The relationship given in Equation 28 was derived for alkali-free  
 714 compositions, though experimental data for Na- and K-bearing compositions in the literature  
 715 are generally consistent with this relationship. Moreover, although it lies outside the scope of  
 716 this review, we note that in hydrothermal fluids the  $\text{Eu}^{2+}$ - $\text{Eu}^{3+}$  equilibrium is 12 times more  
 717 sensitive to pH than to  $\log f\text{O}_2$ , and hence this variable must also be considered in low-  
 718 temperature systems (Brugger et al., 2008).

719

720

## 721 5. Uranium (U)

722

723 Although it has been known for many years that U can exist as  $\text{U}^{4+}$ ,  $\text{U}^{5+}$  and  $\text{U}^{6+}$  in  
 724 silicate melts (e.g. Calas 1979; Schreiber 1983), this fact has often been rather under-  
 725 appreciated in the geochemical literature. The radioactivity of U generates heat as well as a  
 726 series of decay products culminating in Pb, and hence understanding the geochemistry of U is  
 727 particularly important. Interpretation of U-series disequilibrium depends on accurate partition  
 728 coefficients for U and Th (as well as other elements in the series). Because of potential  
 729 differences in redox between mid-oceanic ridges and subduction zone settings, for example, it is  
 730 essential to consider the role of  $f\text{O}_2$  in controlling the partitioning of U relative to Th.

731

732 Partitioning of U as a function of  $f\text{O}_2$  has only been studied for a handful of minerals (Fig.  
 733 7). Despite the importance of garnet in influencing U-series disequilibrium (Beattie, 1993), little  
 734 is known about the how its partitioning of U might be affected by  $f\text{O}_2$ . For all minerals studied to  
 735 date, it appears that  $D_{\text{U}^{4+}} > D_{\text{U}^{5+}} > D_{\text{U}^{6+}}$ . As with the intermediate oxidation states of V, the  
 736 partitioning of  $\text{U}^{5+}$  is difficult to constrain without independent spectroscopic measurements of  
 737  $\text{U}^{5+}/\Sigma\text{U}$  in the same melt composition. An additional complication arises because  $\text{U}^{6+}$  is volatile  
 738 and is gradually lost from 1 atm experiments, leading to uncertainty on  $D_{\text{U}^{6+}}$  because diffusion is  
 739 unlikely to occur fast enough to keep crystals in equilibrium with the changing melt  
 740 composition (Burnham and Berry, 2012).

741

742 Although there are insufficient data to develop a general expression for  $\text{U}^{n+}/\Sigma\text{U}$  as a  
 743 function of melt composition, temperature, pressure and  $f\text{O}_2$ , it is known that higher oxidation  
 744 states are favored by lower temperatures and melts with higher optical basicities (Schreiber,  
 745 1983; Halse, 2014). Notably,  $\text{U}^{5+}$  appears to have a reduced stability field with increasing  
 746 pressure (Halse, 2014): at higher pressure it appears that  $\text{U}^{4+}$  oxidizes directly to  $\text{U}^{6+}$ , leading to  
 747 a sharper change in partition coefficients as a function of  $f\text{O}_2$  (Mallmann et al., 2016).

748

749 U-Pb dating of zircon is widely regarded as one of the most reliable techniques for  
 750 determining rock ages. For zircons younger than a few million years old, it becomes important  
 751 to consider the contribution of  $^{230}\text{Th}$  to the ingrowth of  $^{206}\text{Pb}$ , because minerals for which U is  
 752 less compatible than Th will develop a  $^{206}\text{Pb}$  excess, and vice versa. Correcting for these  
 753 consequences of U-series disequilibrium necessitates estimates of  $D_{\text{Th}}/D_{\text{U}}$ . U is more compatible  
 754 than Th under reducing conditions, but much less compatible at high  $f\text{O}_2$ : the variation in  
 755 terrestrial magmatic redox conditions equates to a  $\sim 100$  kyr range of possible age corrections  
 756 (McLean et al., 2011).

757

758  
759  
760**6. Siderophile elements (Mo, W, Re, Pt group elements)**

761 Siderophile elements (i.e. those with strong tendency to alloy with Fe) are important  
762 tracers of planetary differentiation owing to their propensity of fractionating into planetary  
763 cores. Because of this, a great deal of effort has been made to investigate the behavior of these  
764 elements during core formation and to determine their valence state in silicate melts.

765  
766**6.1. Molybdenum (Mo), tungsten (W) and rhenium (Re)**

767

768 Mo, W and Re are known to occur in 4+ and 6+ valence states at  $fO_2$ s relevant to  
769 planetary magmatism (Cottrell et al., 2009; Ertel et al., 2001; Holzheid et al., 1994; O'Neill &  
770 Eggins, 2002; O'Neill et al., 2008; Righter et al., 2016; Wade et al., 2012; 2013). While the  
771 hexavalent state of Mo, W and Re is dominant over most planetary conditions (Fig. 2), the  
772 mineral/melt partitioning behavior of these elements is strongly controlled by their tetravalent  
773 state (Fig. 8).

774

775 A common feature of the partitioning behavior of Mo, W and Re is that their 4+ valence  
776 state is significantly more compatible in silicates and oxides (e.g. spinel) than their 6+ valence  
777 state, the latter of which being almost perfectly incompatible in crystalline phases. The relative  
778 compatibility in silicates and oxides tends to follow the order  $D_{\text{cpx}} > D_{\text{opx}} > D_{\text{olv}} > D_{\text{spl}} \sim D_{\text{plg}}$ ,  
779 independently of valence state (Fonseca et al., 2014; Leitzke et al., 2016; 2017; Mallmann and  
780 O'Neill, 2007; Wijbrans et al., 2015). For all three elements, the difference between the  
781 mineral/melt partition coefficient of their reduced and oxidized species spans three to five  
782 orders of magnitude (Fig. 8). The difference in partition coefficients between the valence states  
783 is most pronounced for clinopyroxene, with  $D_{6+} \sim 10^{-5}$  and  $D_{4+} \sim 3-6$ . The compatibility of  
784 tetravalent Re, Mo and W in clinopyroxene results from the nearly ideal size of these cations ( $r^{VI}$   
785 = 0.66 Å for  $W^{4+}$ , 0.65 Å for  $Mo^{4+}$  and 0.63 Å for  $Re^{4+}$ ) relative to the octahedral M1 site ( $r_{0^{4+,M1}}$   
786  $\sim 0.66$  Å; Hill et al., 2000), which makes the substitution into clinopyroxene lattice energetically  
787 favorable. While the mineral/melt partitioning of  $Re^{4+}$  and  $Mo^{4+}$  were determined directly by  
788 experimental data at reducing conditions (Mallmann and O'Neill, 2007; Leitzke et al., 2017),  
789 data for  $W^{4+}$  was constrained by Fonseca et al. (2014) using a lattice strain fit to Ti, Hf, Zr and  
790 Re. This is because the extremely reducing conditions necessary to reduce all  $W^{6+}$  to  $W^{4+}$  cannot  
791 be achieved in the laboratory. The important conclusion of these studies is that the partitioning  
792 behavior of these elements in magmatic systems will be completely different depending on  $fO_2$ ,  
793 with significant implications for comparing lunar vs. terrestrial, or oceanic vs. arc magmatism.

794

795 The effect of composition on the mineral/melt partitioning of Mo, W and Re in  
796 pyroxenes has been addressed in some studies. Hill et al. (2000) and Righter and Shearer  
797 (2003) found a negative correlation between  $D_{\text{Mo,W}}$  and the Ca-Tschermak (CaTs) component in  
798 clinopyroxene. However, the opposite trend was found by Leitzke et al. (2017), who observed  
799 that the clinopyroxenes with the highest CaTs reported by Hill et al (2000) were formed from  
800 melt compositions with the highest CaO. Leitzke et al. (2017) speculated that, because the  
801 activity coefficients of  $MoO_3$  and  $MoO_2$  in silicate melts decrease with increasing CaO content  
802 (O'Neill and Eggins, 2002), the negative correlation found by Hill et al. (2000) could be due to  
803 the high CaO content of the silicate melt rather than pyroxene composition. Leitzke et al. (2016)  
804 investigated the effect of  $TiO_2$  in the silicate melt, observing a positive correlation between the  
805  $TiO_2$  content of the melt on the partitioning of  $Mo^{4+}$  and  $W^{4+}$ , but little to no effect on the  
806 partitioning of  $Mo^{6+}$  and  $W^{6+}$  (perhaps because these cations are very incompatible).  
807 Conversely, partitioning coefficients for Hf and Zr decrease with  $TiO_2$  content of the melt. ( $D_{\text{Ti}}$   
808 remained constant, as expected for Henry's Law behavior). Leitzke et al. (2016) argued that the  
809 introduction of  $CaTi^{4+}Al_2O_6$  into clinopyroxene with increasing melt  $TiO_2$  raises elastic strain in  
810

811 the M1 site of clinopyroxene. The increased elastic strain (which results in a tighter parabola)  
 812 leads to an increase in the partitioning values of cations whose size are close to ideal for that  
 813 site (e.g.  $W^{4+}$ ), and a decrease in the partitioning values of those cations whose size are either  
 814 smaller or larger than the ideal for that site (e.g.  $Zr^{4+}$  and  $Hf^{4+}$ ).

815

816

## 817 6.2. Platinum Group Elements (Ru, Rh, Pd, Os, Ir, Pt)

818

819 There have been few studies investigating the redox-dependent partitioning behavior of  
 820 the Platinum Group Elements (PGE) during magmatism, with most focusing on the role of base  
 821 metal sulfides and, to a lesser extent, oxides. The scarcity of partitioning data arises from the  
 822 low solubility of PGE in silicate melts (typically  $< a few \mu\text{g/g}$ ), especially under reducing  
 823 conditions (O'Neill et al., 1995), and from the almost unavoidable presence of sub-micrometer  
 824 metallic nuggets that plague the analyses of PGEs in synthetic silicate glasses and often lead to  
 825 erroneous solubility values (Ertel et al., 2008). The solubility of a PGE in a silicate melt in  
 826 equilibrium with metal can give an indication of its valence state(s), as it will dissolve according  
 827 to Equation 10 (with  $x = 0$  for the metal). However, despite significant effort in the last 20-30  
 828 years, PGE solubility results are still controversial. This leads to ambiguous interpretations  
 829 regarding the PGE speciation as a function of  $fO_2$ . For example, solubility data for Ru are used to  
 830 indicate that it either dissolves as  $Ru^{3+}$  (Borisov and Nachtweyh, 1998), or as both  $Ru^{3+}$  and  
 831  $Ru^{4+}$  (Laurenz et al., 2013) in silicate melts over planetary magmatic  $fO_2$ s. Similarly, Os appears  
 832 to dissolve as  $Os^{3+}$  under most conditions, though the possibility of  $Os^{4+}$  being stable at more  
 833 oxidizing conditions cannot be ruled out (Borisov and Walker, 2000; Fortenfant et al., 2006).  
 834 Data for Ir are also ambiguous, indicating speciation as either  $Ir^{3+}$ , or combinations of  $Ir^{1+}$  -  $Ir^{3+}$   
 835 or  $Ir^{2+}$  -  $Ir^{3+}$  (Brenan et al., 2005; Borisov and Palme, 1995; Fonseca et al., 2011; O'Neill, 2015).  
 836 Pt appears to occur exclusively as  $Pt^{2+}$ , except perhaps at very oxidizing conditions ( $FMQ > 5$ )  
 837 where  $Pt^{4+}$  may also be stable (Ertel et al., 1999). Of all PGEs, unambiguous evidence of redox-  
 838 sensitivity over magmatic  $fO_2$ s only exists for palladium and rhodium, both of which occur as  
 839 monovalent and divalent cations under typical magmatic  $fO_2$ s (e.g. Laurenz et al., 2010;  
 840 Sommer, 2014; Fig. 2). Reports of other valence states for Pd and Rh in the literature arise from  
 841 interpretation of micro(nano)nugget contaminated data (e.g. Borisov et al., 1994; Ertel et al.,  
 842 1999).

843

844 Of the common magmatic minerals, spinel is the only mineral capable of accommodating  
 845 significant amounts of PGEs, particularly Ru, Ir and Rh (e.g. Park et al., 2017). Wijbrans et al.,  
 846 (2015) reported a marked increase in  $D_{Rh}$  around FMQ in both Fe-free and Fe-rich spinels,  
 847 indicating higher compatibility of  $Rh^{3+}$  relative to  $Rh^{2+}$ . Brenan et al. (2012) observed  
 848 significant variations in the partitioning of several PGEs with  $fO_2$  for Fe- and Cr-bearing spinels.  
 849 However, as noted above, the partitioning of trace elements into magnetite is controlled by the  
 850  $Fe^{3+}$  and  $Fe^{2+}$  content of the melt, and it is often difficult to deconvolve this effect, and that of  
 851 drastically changing site occupancies in the spinel from that of valence state changes in the trace  
 852 element of interest. Nevertheless, the data in the Fe-free system are consistent with a change  
 853 from  $Rh^+$  to  $Rh^{2+}$ , and also with olivine/melt partitioning data that shows decreasing  $D_{Rh}$  with  
 854 increasing  $fO_2$  (Brenan et al., 2003). Of the very few spinel/melt partitioning data available, Pd  
 855 appears to be incompatible in spinel (Brenan et al., 2012).

856

857

## 858 7. Concluding remarks

859

860 In this chapter we have shown that the partitioning behavior of redox-sensitive trace  
 861 elements will almost inevitably change with  $fO_2$  in magmatic systems. This is because the  
 862 incorporation of cations into crystal lattices (at constant pressure, temperature and  
 863 composition) depends on their charge, size, and crystal-field stabilization energies, all of which

864 likely vary substantially between the oxidized and reduced species of the same element. This  
865 dependence on  $fO_2$  means that petrologic/geochemical modelling involving elements such as Ti,  
866 Cr, V, Ce, Eu, U, Mo, Re, W, Pd, Rh (and probably others) must account for the oxidation state of  
867 the magma. As the only major-component redox-sensitive elements in many magmatic systems,  
868 the partitioning behavior of Fe is more likely to control rather than to reflect  $fO_2$ . Given the large  
869 range (10-15 order of magnitude; Fig. 2) of magmatic  $fO_2$  in planetary systems, significant  
870 differences in the partitioning behavior of individual elements ought to be expected. For  
871 instance, several studies have shown that certain trace elements behave in completely different  
872 ways during lunar compared to terrestrial magmatism, or during magmatism in mid-ocean  
873 ridge compared to subduction zone settings.

874  
875 Nevertheless, if the partitioning of redox-sensitive trace elements is determined  
876 experimentally as a function of  $fO_2$  (and the effects of other parameters such as pressure,  
877 temperature and composition accounted for), then partitioning relations preserved in natural  
878 samples (e.g. glass and phenocryst in a volcanic rock) may provide useful ways of estimating the  
879 oxidation state of magmatic systems. This approach has the greatest advantage of being  
880 insensitive to late-stage degassing, charge-transfer (electron-exchange) reactions, or surficial  
881 alteration, all of which may potentially alter other magmatic redox proxies (e.g.  $Fe^{3+}/\Sigma Fe$ ).

882  
883 The preceding discussion demonstrates the importance of a good understanding of  
884 redox in modelling or interpreting trace element concentrations in melts and minerals.  
885 However, it should also be apparent that further work is required to bring our ability to model  
886 the partitioning of redox-variable elements. First, there are several elements for which very  
887 little information is available: most notably the PGEs, which have been investigated in  
888 surprisingly few minerals and whose redox transitions are poorly constrained. Copper was  
889 excluded from this review because of a paucity of data, but the data of Liu et al. (2014, 2015)  
890 indicate that its partitioning changes significantly from FMQ+1 to FMQ+5, a range that is highly  
891 relevant to arc environments where essentially all the world's economic Cu deposits are located.  
892 Likewise, experimental partitioning data by Mallmann and O'Neill (2009) indicate a potential  
893 change of phosphorus valence states from 5+ to 3+ under conditions below FMQ-4, but the  
894 results could also be explained by volatility loss from the melt after crystallization. And, under  
895 ultra-reducing conditions ( $\sim$  FMQ-7), where Nb and Ta begin to show siderophile tendencies,  
896 there is evidence that they may take on lower valence states in silicate melts (Cartier et al.,  
897 2014).

898  
899 Furthermore, the dependence of these redox transitions and partition coefficients on  
900 temperature and melt composition is complex, and only partially understood for the majority of  
901 the redox couples addressed here. As seen in Figure 4, melt composition affects the partitioning  
902 of different oxidation states of the same element in differing ways, an effect that is additional to  
903 the influence of stoichiometric controls on trace element partitioning. Similarly, melt  
904 compositional effects can shift the redox transition by up to 6 log units of  $fO_2$  (Fig. 2). Because of  
905 these complications, extreme caution should be taken when attempting to study partitioning of  
906 redox-variable elements outside their calibrated ranges.

907  
908 Many factors are important in selecting a mineral/melt partitioning oxybarometer. First,  
909 the anticipated redox state of the system will give an indication of which redox couples are  
910 relevant, but a large contrast between the compatibilities of the valence states of the element  
911 can sufficiently outweigh this consideration (for example, zircon will develop a Ce anomaly at  
912 conditions that are many orders of magnitude more reducing than the midpoint of the  $Ce^{3+}$ - $Ce^{4+}$   
913 equilibrium). The figures presented in this chapter may guide the geoscientist in determining  
914 whether the partition coefficient is likely to be sensitive to  $fO_2$  for her or his samples. As  
915 emphasized above, the availability of appropriate experimental constraints is important, as are  
916 more general petrological considerations, for instance resistance to alteration processes such as

917 diffusive re-equilibration. In the ideal case, multiple elements and minerals would be combined  
918 to check for internal consistency.

919

920

## 921 Acknowledgments

922

923 We thank Aaron Bell and Roberto Moretti for their constructive comments. G.M.  
924 acknowledges funding of a Discovery Early Career Research Award from the Australian  
925 Research Council – ARC (grant DE160100169), A.B. acknowledges support from the ARC (grant  
926 FL130100066) and R.O.C.F. acknowledges funding of a Heisenberg Fellowship from the German  
927 Research Council – DFG (grants FO 698/5-1 and FO 698/11-1).

928

929

## 930 References

931

932 Aigner-Torres, M., Blundy, J., Ulmer, P., & Pettke, T. (2007). Laser ablation ICPMS study of trace  
933 element partitioning between plagioclase and basaltic melts: An experimental approach.  
934 *Contributions to Mineralogy and Petrology*, 153, 647-667.

935 Allen, J.M., Grossman, L., Davis, A.M., & Hutcheon, I.D. (1978). Mineralogy, textures and mode of  
936 formation of a hibonite-bearing Allende inclusion. 9<sup>th</sup> Lunar and Planetary Science  
937 Conference, 1209-1233.

938 Arató, R., & Audétat, A. (2017). Experimental calibration of a new oxybarometer for silicic  
939 magmas based on the vanadium partitioning between magnetite and silicate melt.  
940 *Geochimica et Cosmochimica Acta*, 209, 284-295.

941 Bachmann, O., Dungan, M.A., & Bussy, F. (2005). Insights into shallow magmatic processes in  
942 large silicic magma bodies: The trace element record in the Fish Canyon magma body,  
943 Colorado. *Contributions to Mineralogy and Petrology*, 149, 338-349.

944 Barnes, S.J. (1986). The distribution of chromium among orthopyroxene, spinel and silicate  
945 liquid at atmospheric pressure. *Geochimica et Cosmochimica Acta*, 50, 1889-1909.

946 Beattie, P. (1993). Uranium–thorium disequilibria and partitioning on melting of garnet  
947 peridotite. *Nature*, 363, 63-65.

948 Bell, A.S., Burger, P.V., Le, L., Shearer, C.K., Papike, J.J., Sutton, S.R., Newville, M., & Jones, J.  
949 (2014). XANES measurements of Cr valence in olivine and their application to planetary  
950 basalts. *American Mineralogist*, 99, 1404-1412.

951 Berry, A.J., & O'Neill, H.St.C. (2004). A XANES study of the oxidation state of chromium in silicate  
952 glasses. *American Mineralogist*, 89, 790-798.

953 Berry, A.J., O'Neill, H.St.C., Scott, D.R., Foran, G.J., & Shelley, J.M.G. (2006). The effect of  
954 composition on Cr<sup>2+</sup>/Cr<sup>3+</sup> in silicate melts. *American Mineralogist*, 91, 1901-1908.

955 Berry, A.J., Schofield, P.F., Kravtsova, A.N., Miller, L.A., Stephen, N.R., Walker, A.M., Soldatov, A.V.,  
956 Ireland, T.R., Geraki, K. & Mosselmans, J.F.W. (2017). The limitations of hibonite as a single-  
957 mineral oxybarometer for early solar system processes. *Chemical Geology*, 466, 32-40.

958 Berry, A.J., Shelley, J.M.G., Foran, G.J., O'Neill, H.St.C., & Scott, D.R. (2003). A furnace design for  
959 XANES spectroscopy of silicate melts under controlled oxygen fugacities and temperatures to  
960 1773 K. *Journal of Synchrotron Radiation*, 10, 332-336.

961 Blundy J., & Wood, B. (1994). Prediction of crystal-melt partition coefficients from elastic  
962 moduli. *Nature*, 372, 452-454.

963 Borisov, A.A. (2012). The Ti<sup>4+</sup>/Ti<sup>3+</sup> ratio of magmatic melts: application to the problem of the  
964 reduction of lunar basalts. *Petrology* 20, 391-398.

- 965 Borisov, A.A., Kadik, A.A., Zharkova, Ye., & Kalinichenko, N.V. (1987). Effects of oxygen fugacity  
966 on the ratio between valency forms of vanadium in magmas. *Geokhimiya*, 7, 915-920.
- 967 Borisov, A., & Nachtweyh, K. (1998). Ru solubility in silicate melts: experimental results in  
968 oxidizing region. 29<sup>th</sup> Lunar and Planetary Science Conference, 1320.
- 969 Borisov, A., & Palme, H. (1995). The solubility of iridium in silicate melts: new data from  
970 experiments with Ir<sub>10</sub>Pt<sub>90</sub> alloys. *Geochimica et Cosmochimica Acta*, 59, 481-485.
- 971 Borisov, A., & Walker, R. J. (2000). Os solubility in silicate melts: New efforts and results.  
972 *American Mineralogist*, 85, 912-917.
- 973 Borisov, A., Palme, H., & Spettel, B. (1994). Solubility of palladium in silicate melts: Implications  
974 for core formation in the Earth. *Geochimica et Cosmochimica Acta*, 58, 705-716.
- 975 Brenan, J. M., Finnigan, C. F., McDonough, W. F., & Homolova, V. (2012). Experimental  
976 constraints on the partitioning of Ru, Rh, Ir, Pt and Pd between chromite and silicate melt:  
977 The importance of ferric iron. *Chemical Geology*, 302, 16-32.
- 978 Brenan, J. M., McDonough, W. F., & Ash, R. (2005). An experimental study of the solubility and  
979 partitioning of iridium, osmium and gold between olivine and silicate melt. *Earth and  
980 Planetary Science Letters*, 237, 855-872.
- 981 Brenan, J. M., McDonough, W. F., & Dalpe, C. (2003). Experimental constraints on the  
982 partitioning of rhenium and some platinum-group elements between olivine and silicate  
983 melt. *Earth and Planetary Science Letters*, 212, 135-150.
- 984 Brugger, J., Etschmann, B., Pownceby, M., Liu, W., Grundler, P., & Brewe, D. (2008). Oxidation  
985 state of europium in scheelite: Tracking fluid–rock interaction in gold deposits. *Chemical  
986 Geology*, 257, 26-33.
- 987 Burgisser, A., & Scaillet, B. (2007). Redox evolution of a degassing magma rising to the surface.  
988 *Nature*, 445, 194-197.
- 989 Burnham, A.D., & Berry, A.J. (2017). Formation of Hadean granites by melting of igneous crust.  
990 *Nature Geoscience*, 10, 457-461.
- 991 Burnham, A.D., & Berry, A.J. (2012). An experimental study of trace element partitioning  
992 between zircon and melt as a function of oxygen fugacity. *Geochimica et Cosmochimica Acta*,  
993 95, 196-212.
- 994 Burnham, A.D., & Berry, A.J. (2014). The effect of oxygen fugacity, melt composition,  
995 temperature and pressure on the oxidation state of cerium in silicate melts. *Chemical  
996 Geology*, 366, 52-60.
- 997 Burnham, A.D., Berry, A.J., Halse, H.R., Schofield, P.F., Cibin, G., & Mosselmans, J.F.W. (2015). The  
998 oxidation state of europium in silicate melts as a function of oxygen fugacity, composition  
999 and temperature. *Chemical Geology*, 411, 248-259.
- 1000 Burns, R.G. (1975). On the occurrence and stability of divalent chromium in olivine included in  
1001 diamonds. *Contributions to Mineralogy and Petrology*, 51, 213-221.
- 1002 Burns, R.G. (1993). *Mineralogical applications of crystal field theory*. 2<sup>nd</sup> Edition, Cambridge  
1003 University Press, 551 p.
- 1004 Burns, R.G., & Burns, V.M. (1984). Crystal chemistry of meteoritic hibonites. *Journal of  
1005 Geophysical Research*, 89, 313-321.
- 1006 Burns, R.G., Huggins, F.E. & Abu-Eid, R.M. (1972). Polarized absorption spectra of single crystals  
1007 of lunar pyroxenes and olivines. *The Moon*, 4, 93-102.
- 1008 Burns, V.M., & Burns, R.G. (1975). Mineralogy of chromium. *Geochimica et Cosmochimica Acta*,  
1009 39, 903-910.

- 1010 Calas, G. (1979). Etude expérimentale du comportement de l'uranium dans les magmas: États  
1011 d'oxydation et coordinance. *Geochimica et Cosmochimica Acta*, 43, 1521-1531.
- 1012 Canil, D. (1997). Vanadium partitioning and the oxidation state of Archaean komatiite magmas.  
1013 *Nature*, 389, 842-845.
- 1014 Canil, D. (1999). Vanadium partitioning between orthopyroxene, spinel and silicate melt and the  
1015 redox states of mantle source regions for primary magmas. *Geochimica et Cosmochimica*  
1016 *Acta*, 63, 557-572.
- 1017 Canil, D. (2002). Vanadium in peridotites, mantle redox and tectonic environments: Archean to  
1018 present. *Earth and Planetary Science Letters*, 195, 75-90.
- 1019 Canil, D., & Fedortchouk, Y. (2000). Clinopyroxene-liquid partitioning for vanadium and the  
1020 oxygen fugacity during the formation of cratonic and oceanic mantle lithosphere. *Journal of*  
1021 *Geophysical Research*, 105, 26003-26016.
- 1022 Canil, D., & Fedortchouk, Y. (2001). Olivine-liquid partitioning of vanadium and other trace  
1023 elements, with applications to modern and ancient picrites. *Canadian Mineralogist*, 39, 319-  
1024 330.
- 1025 Canil, D. (1999). Vanadium partitioning between orthopyroxene, spinel and silicate melt and  
1026 the redox states of mantle source regions for primary magmas. *Geochimica et Cosmochimica*  
1027 *Acta*, 63, 557-572.
- 1028 Cartier, C., Hammouda, T., Boyet, M., Mathon, O., Testemale, D., & Moine, B.N. (2015). Evidence  
1029 for Nb<sup>2+</sup> and Ta<sup>3+</sup> in silicate melts under highly reducing conditions: A XANES study.  
1030 *American Mineralogist*, 100, 2152-2158.
- 1031 Cottrell, E., Walter, M.J., & Walker, D., (2009). Metal-silicate partitioning of tungsten at high  
1032 pressure and temperature: Implications for equilibrium core formation in Earth. *Earth*  
1033 *Planetary Science Letters*, 281, 275-287
- 1034 de Moor, J.M., Fischer, T.P., Sharp, Z.D., King, P.L., Wilke, M., Botcharnikov, R.E., Cottrell, E.,  
1035 Zelenski, M., Marty, B., Klimm, K., Rivard, C., Ayalew, D., Ramirez, C., & Kelley, K.A. (2013).  
1036 Sulfur degassing at Erta Ale (Ethiopia) and Masaya (Nicaragua) volcanoes: Implications for  
1037 degassing processes and oxygen fugacities of basaltic systems. *Geochemistry, Geophysics,*  
1038 *Geosystems*, 14, doi: 10.1002/ggge.20255
- 1039 Dohmen, R., & Blundy, J. (2014). A predictive thermodynamic model for element partitioning  
1040 between plagioclase and melt as a function of pressure, temperature and composition.  
1041 *American Journal of Science*, 314, 1319-1372.
- 1042 Doyle, P.M., Schofield, P.F., Berry, A.J., Walker, A.M., & Knight, K.S. (2014). Substitution of Ti<sup>3+</sup>  
1043 and Ti<sup>4+</sup> in hibonite (CaAl<sub>12</sub>O<sub>19</sub>). *American Mineralogist*, 99, 1369-1382.
- 1044 Duffy, J.A. (1993). A review of optical basicity and its applications to oxidic systems. *Geochimica*  
1045 *et Cosmochimica Acta*, 57, 3961-3970.
- 1046 Eeckhout, S.G., Bolfan-Casanov, N., McCammon C., Klemme, S., & Amiguet, E. (2007). XANES  
1047 study of the oxidation state of Cr in lower mantle phases: Periclase and magnesium silicate  
1048 perovskite. *American Mineralogist*, 92, 966-972.
- 1049 Ertel W., O'Neill H.St.C., Sylvester P.J., Dingwell D.B., & Spettel B. (2001). The solubility of  
1050 rhenium in silicate melts: Implications for the geochemical properties of rhenium at high  
1051 temperatures. *Geochimica et Cosmochimica Acta*, 65, 2161-2170
- 1052 Ertel, W., Dingwell, D. B., & Sylvester, P. J. (2008). Siderophile elements in silicate melts — A  
1053 review of the mechanically assisted equilibration technique and the nanonugget issue.  
1054 *Chemical Geology*, 248, 119-139.

- 1055 Ertel, W., O'Neill, H.St.C., Sylvester, P. J., & Dingwell, D.B. (1999). Solubilities of Pt and Rh in a  
1056 haplobasaltic silicate melt at 1300 °C. *Geochimica et Cosmochimica Acta*, 63, 2439-2449.
- 1057 Fonseca, R.O.C., Mallmann, G., O'Neill, H.St.C., Campbell, I. H., & Laurenz, V. (2011). Solubility of  
1058 Os and Ir in sulfide melt: Implications for Re/Os fractionation during mantle melting. *Earth  
1059 and Planetary Science Letters*, 311, 339-350.
- 1060 Fonseca, R.O.C., Mallmann, G., Sprung, P., Sommer, J.E., Heuser, A., Speelmanns, I.M., & Blanchard,  
1061 H. (2014). Redox controls on tungsten and uranium crystal/silicate melt partitioning and  
1062 implications for the U/W and Th/W ratio of the lunar mantle. *Earth and Planetary Science  
1063 Letters*, 404, 1-13.
- 1064 Fortenfant, S.S., Dingwell, D.B., Ertel-Ingrisch, W., Capmas, F., Birck, J.L., & Dalpe, C. (2006).  
1065 Oxygen fugacity dependence of Os solubility in haplobasaltic melt. *Geochimica et  
1066 Cosmochimica Acta*, 70, 742-756.
- 1067 Fraser, D.G. (1975). Activities of trace elements in silicate melts. *Geochimica et Cosmochimica  
1068 Acta*, 39, 1525-1530.
- 1069 Frost, D.J., Liebske, C., Langenhorst, F., McCammon, C.A., Tronnes, R.G., & Rubie, D.C. (2004).  
1070 Experimental evidence for the existence of iron-rich metal in the Earth's lower mantle.  
1071 *Nature*, 428, 409-412.
- 1072 Gerdes, A., Kogarko, L.N., & Vladykin, N.V. (2017). New data on the age and nature of the Khan-  
1073 Bogt alkaline granites, Mongolia. *Doklady Earth Sciences*, 477, 1320-1324.
- 1074 Grossman, L., Beckett, J.R., Fedkin, A.V., Simon, S.B., & Cieslan, F.J. (2008). Redox conditions in  
1075 the solar nebula: Observational, experimental, and theoretical calculations. *Reviews in  
1076 Mineralogy and Geochemistry*, 68, 93-140.
- 1077 Halse, H.R. (2014). *Using synchrotron radiation to determine the oxidation state of uranium in  
1078 magmas*. PhD thesis, Imperial College London (<http://hdl.handle.net/10044/1/19423>).
- 1079 Hanson, B., & Jones, J.H. (1998). The systematics of Cr<sup>3+</sup> and Cr<sup>2+</sup> partitioning between olivine  
1080 and liquid in the presence of spinel. *American Mineralogist*, 83, 669-684.
- 1081 Hastie, A.R., Kerr, A.C., Mitchell, S.F., & Millar, I.L. (2009). Geochemistry and tectonomagmatic  
1082 significance of lower Cretaceous island arc lavas from the Devils Racecourse Formation,  
1083 eastern Jamaica. *Geological Society London, Special Publications*, 328, 339-360.
- 1084 Hill, E., Wood, B.J., & Blundy, J.D. (2000). The effect of Ca-Tschermaks component on trace  
1085 element partitioning between clinopyroxene and silicate melt. *Lithos*, 53, 203-215.
- 1086 Holzheid, A., Borisov, A., & Palme, H. (1994). The effect of oxygen fugacity and temperature on  
1087 solubilities of nickel, cobalt and molybdenum in silicate melts. *Geochimica et  
1088 Cosmochimica Acta*, 58, 1975-1981
- 1089 Jaques, A.L. (2016). Major and trace element variations in oxide and titanate minerals in the  
1090 West Kimberley lamproites, Western Australia. *Mineralogy and Petrology*, 110, 159-197.
- 1091 Jollands, M.C., O'Neill, H.St.C., Van Orman, J., Berry, A.J., Hermann, J., Newville, M., & Lanzirrotti, A.  
1092 (2018). Substitution and diffusion of Cr<sup>2+</sup> and Cr<sup>3+</sup> in synthetic forsterite and natural olivine  
1093 at 1200-1500 °C and 1 bar. *Geochimica et Cosmochimica Acta*, 220, 407-428.
- 1094 Karner, J.M., Papike, J.J., Shearer, C.K., McKay, G., Le, L., and Burger, P. (2007). Valence state  
1095 partitioning of Cr and V between pyroxene-melt: Estimates of oxygen fugacity for martian  
1096 basalt QUE 94201. *American Mineralogist*, 92, 1238-1241.
- 1097 Karner, J.M., Papike, J.J., Sutton, S.R., Shearer, C.K., Burger, P., McKay, G., & Le, L. (2008). Valence  
1098 state partitioning of V between pyroxene-melt: Effects of pyroxene and melt composition,  
1099 and direct determination of V valence states by XANES. Application to Martian QUE 94201  
1100 composition. *Meteoritics & Planetary Science*, 43, 1275-1285.

- 1101 Kesson, S.E., Fitzgerald, J.D., Shelley, J.M.G., & Withers, R.L. (1995). Phase relations, structure and  
1102 crystal chemistry of some aluminous silicate perovskites. *Earth and Planetary Science*  
1103 *Letters*, 134, 187-201.
- 1104 Kimata, M. (1988). The crystal structure of non-stoichiometric Eu-anorthite: An explanation of  
1105 the Eu-positive anomaly. *Mineralogical Magazine*, 52, 257-265.
- 1106 King, P.L., Hervig, R.L., Holloway, J.R., Delaney, J.S., & Dyar, M.D. (2000). Partitioning of  
1107  $\text{Fe}^{3+}/\text{Fe}_{\text{total}}$  between amphibole and basanitic melt as a function of oxygen fugacity. *Earth and*  
1108 *Planetary Science Letters*, 178, 97-112.
- 1109 Klemme, S., & O'Neill, H.St.C. (2000). The effect of Cr on the solubility of Al in orthopyroxene:  
1110 Experiments and thermodynamic modelling. *Contributions to Mineralogy and Petrology*,  
1111 140, 84-98.
- 1112 Krawczynski, M.J., Grove, T.L. & Behrens, H. (2012). Amphibole stability in primitive arc  
1113 magmas: Effects of temperature,  $\text{H}_2\text{O}$  content, and oxygen fugacity. *Contributions to*  
1114 *Mineralogy and Petrology*, 164, 317-339.
- 1115 Kuehner, S.M., Laughlin, J.R., Grossman, L., Johnson, M.L. & Burnett, D.S. (1989). Determination  
1116 of trace element mineral/liquid partition coefficients in melilite and diopside by ion and  
1117 electron microprobe techniques. *Geochimica et Cosmochimica Acta*, 53, 3115-3130.
- 1118 Laubier, M., Grove, T.L., & Langmuir, C.H. (2014). Trace element mineral/melt partitioning for  
1119 basaltic and basaltic andesitic melts: An experimental and laser ablation ICP-MS study with  
1120 application to the oxidation state of mantle source regions. *Earth and Planetary Science*  
1121 *Letters*, 392, 265-278.
- 1122 Laurenz, V., Fonseca, R.O.C., Ballhaus, C., & Sylvester, P. J. (2010), Solubility of palladium in  
1123 picritic melts: 1. The effect of iron. *Geochimica et Cosmochimica Acta*, 74, 2989-2998.
- 1124 Laurenz, V., Fonseca, R.O.C., Ballhaus, C., Jochum, K. P., Heuser, A., & Sylvester, P. J. (2013). The  
1125 solubility of palladium and ruthenium in picritic melts: 2. The effect of sulfur. *Geochimica et*  
1126 *Cosmochimica Acta*, 108, 172-183.
- 1127 Law, K.M., Blundy, J.D., Wood, B.J., & Ragnarsdottir, K.V. (2000). Trace element partitioning  
1128 between wollastonite and silicate-carbonate melt. *Mineralogical Magazine*, 64, 651-661.
- 1129 Leitzke, F.P., Fonseca, R.O.C., Michely, L.T., Sprung, P., Münker, C., Heuser, A., & Blanchard, H.  
1130 (2016), The effect of titanium on the partitioning behavior of high-field strength elements  
1131 between silicates, oxides and lunar basaltic melts with applications to the origin of mare  
1132 basalts. *Chemical Geology*, 440, 219–238
- 1133 Leitzke, F.P., Fonseca, R.O.C., Sprung, P., Mallmann, G., Lagos, M., Michely, L.T. & Münker, C.  
1134 (2017). Redox dependent behaviour of molybdenum during magmatic processes in the  
1135 terrestrial and lunar mantle: Implications for the Mo/W of the bulk silicate Moon. *Earth and*  
1136 *Planetary Science Letters*, 474, 503-515.
- 1137 Leitzke, F.P., Fonseca, R.O.C., Göttlicher, J., Steininger, R., Jahn, S., Prescher, C., & Lagos, M.  
1138 (2018). Ti K-edge XANES study on the coordination number and oxidation state of titanium  
1139 in pyroxene, olivine, armalcolite, ilmenite, and silicate glass during mare basalt petrogenesis.  
1140 *Contributions to Mineralogy and Petrology*, 173, 103.
- 1141 Li, J.P., O'Neill, H.St.C. & Seifert, F. (1995). Subsolvus phase relations in the system  $\text{MgO-SiO}_2\text{-Cr}$ -  
1142  $\text{O}$  in equilibrium with metallic Cr, and their significance for the petrochemistry of chromium.  
1143 *Journal of Petrology*, 36, 107-132.
- 1144 Liu, X., & O'Neill, H.St.C. (2004). The effect of  $\text{Cr}_2\text{O}_3$  on the partial melting of spinel-lherzolite in  
1145 the system  $\text{CaO-MgO-Al}_2\text{O}_3\text{-SiO}_2\text{-Cr}_2\text{O}_3$  at 1.1 GPa. *Journal of Petrology*, 45, 2261-2286.

- 1146 Liu, X., Xiong, X., Audétat, A., Li, Y., Song, M., Li, L., Sun, W., & Ding, X. (2014). Partitioning of  
1147 copper between olivine, orthopyroxene, clinopyroxene, spinel, garnet and silicate melts at  
1148 upper mantle conditions. *Geochimica et Cosmochimica Acta*, 125, 1-22.
- 1149 Liu, X., Xiong, X., Audétat, A., & Li, Y. (2015). Partitioning of Cu between mafic minerals, Fe-Ti  
1150 oxides and intermediate to felsic melts. *Geochimica et Cosmochimica Acta*, 151, 86-102.
- 1151 Longhi, J., Walker, D., & Hays, J.F. (1976). Fe and Mg in plagioclase. 7<sup>th</sup> Lunar and Planetary  
1152 Science Conference, 1281-1300.
- 1153 Lundgaard, K.L., & Tegner, C. (2004). Partitioning of ferric and ferrous iron between plagioclase  
1154 and silicate melt. *Contributions to Mineralogy and Petrology*, 147, 470-483.
- 1155 Ma, C., & Rossman, G.R. (2009). Grossmanite, CaTi<sup>3+</sup>AlSiO<sub>6</sub>, a new pyroxene from the Allende  
1156 meteorite. *American Mineralogist*, 94, 1491-1494.
- 1157 Mallmann, G., & O'Neill, H.St.C. (2007). The effect of oxygen fugacity on the partitioning of Re  
1158 between crystals and silicate melt during mantle melting. *Geochimica et Cosmochimica Acta*,  
1159 71, 2837-2857.
- 1160 Mallmann, G., & O'Neill, H.St.C. (2009). The crystal/melt partitioning of V during mantle melting  
1161 as a function of oxygen fugacity compared with some other elements (Al, P, Ca, Sc, Ti, Cr, Fe,  
1162 Ga, Y, Zr and Nb). *Journal of Petrology*, 50, 1765-1794.
- 1163 Mallmann, G., & O'Neill, H.St.C. (2013). Calibration of an empirical thermometer and  
1164 oxybarometers based on the partitioning of Sc, Y and V between olivine and silicate melt.  
1165 *Journal of Petrology*, 54, 933-949.
- 1166 Mallmann, G., Wykes, J., Berry, A.J., O'Neill, H.St.C., Cline II, C.J., Turner, S., & Rushmer, T.A.  
1167 (2016). In situ XANES of U and Th in silicate liquids at high pressure and temperature.  
1168 American Geophysical Union, Fall Meeting 2015, abstract MR13A-2418.
- 1169 Mann, U., Marks, M., & Markl, G. (2006). Influence of oxygen fugacities on mineral compositions  
1170 in peralkaline melts: The Katzenbuckel volcano, Southwest Germany. *Lithos*, 91, 262-285.
- 1171 Martel, C., Pichavant, M., Holtz, F., Scaillet, B., Bourdier, J.L., & Traineau, H. (1999). Effects of fO<sub>2</sub>  
1172 and H<sub>2</sub>O on andesite phase relations between 2 and 4 kbar. *Journal of Geophysical Research:*  
1173 *Solid Earth*, 104, 29453-29470.
- 1174 Mathez, E.A. (1984). Influence of degassing on oxidation states of basaltic magmas. *Nature*, 310,  
1175 371-375.
- 1176 McCammon, C. (1997). Perovskite as a possible sink for ferric iron in the lower mantle. *Nature*,  
1177 387, 694-696.
- 1178 McCammon, C. (2005). The paradox of mantle redox. *Science*, 308, 807-808.
- 1179 McCanta, M.C., Dyar, M.D., Rutherford, M.J., & Delaney, J.S. (2004). Iron partitioning between  
1180 basaltic melts and clinopyroxene as a function of oxygen fugacity. *American Mineralogist*, 89,  
1181 1685-1693.
- 1182 McLean, N.M., Bowring, J.F., & Bowring, S.A. (2011). An algorithm for U-Pb isotope dilution data  
1183 reduction and uncertainty propagation. *Geochemistry, Geophysics, Geosystems*, 12, Q0AA18.
- 1184 Moussallam, Y., Edmonds, M., Scaillet, B., Peters, N., Gennaro, E., Sides, I., & Oppenheimer, C.  
1185 (2016). The impact of degassing on the oxidation state of basaltic magmas: A case study of  
1186 Kilauea volcano. *Earth and Planetary Science Letters*, 450, 317-325.
- 1187 Murphy, M.D., Sparks, R.S.J., Barclay, J., Carroll, M.R., Lejeune, A.M., Brewer, T.S., MacDonald, R.,  
1188 Black, S., & Young, S. (1998). The role of magma mixing in triggering the current eruption at  
1189 the Soufriere Hills Volcano, Montserrat, West Indies. *Geophysical Research Letters*, 25, 3433-  
1190 3436.

- 1191 O'Neill, H.St.C. (1987). Quartz-fayalite-iron and quartz-fayalite-magnetite equilibria and the free  
1192 energy of formation of fayalite ( $\text{Fe}_2\text{SiO}_4$ ) and magnetite ( $\text{Fe}_3\text{O}_4$ ). *American Mineralogist*, 72,  
1193 67-75.
- 1194 O'Neill, H.St.C. (2015). The effect of sulfide dissolved in silicate melts on enhancing the solubility  
1195 of the Highly Siderophile Elements. American Geophysical Union, Fall Meeting 2015, abstract  
1196 V52A-04.
- 1197 O'Neill, H.St.C. (2016). The smoothness and shapes of chondrite-normalized rare earth element  
1198 patterns in basalts. *Journal of Petrology*, 57, 1463-1508.
- 1199 O'Neill, H.St.C., & Eggins, S.M. (2002). The effect of melt composition on trace element  
1200 partitioning: An experimental investigation of the activity coefficients of FeO, NiO, CoO, MoO<sub>2</sub>  
1201 and MoO<sub>3</sub> in silicate melts. *Chemical Geology*, 186, 151-181.
- 1202 O'Neill, H.St.C., & Navrotsky, A. (1984). Cations distributions and thermodynamic properties of  
1203 binary spinel solid solutions. *American Mineralogist*, 69, 733-753.
- 1204 O'Neill, H.St.C., Berry, A.J., & Eggins, S.M. (2008). The solubility and oxidation state of tungsten in  
1205 silicate melts: Implications for the comparative chemistry of W and Mo in planetary  
1206 differentiation processes. *Chemical Geology*, 255, 346-359
- 1207 O'Neill, H.St.C., Dingwell, D.B., Borisov, A., Spettel, B., & Palme, H. (1995). Experimental  
1208 petrochemistry of some highly siderophile elements at high temperatures, and some  
1209 implications for core formation and the mantle's early history. *Chemical Geology*, 120, 255-  
1210 273.
- 1211 O'Neill, H.St.C., McCammon, C., Canil, D., Rubie, D.C., Ross, C.R., & Seifert, F. (1993). Mössbauer  
1212 spectroscopy of mantle transition zone phases and determination of minimum Fe<sup>3+</sup> content.  
1213 *American Mineralogist*, 78, 456-460.
- 1214 Ohashi, H., Fujita, T. & Osawa, T. (1982). The crystal structure of NaTiSi<sub>2</sub>O<sub>6</sub> pyroxene. *The*  
1215 *Journal of the Japanese Association of Mineralogists, Petrologists and Economic Geologists*,  
1216 77, 305-309.
- 1217 Ottonello, G., Moretti, R., Marini, L. & Zuccolini, M.V. (2001). Oxidation state of iron in silicate  
1218 glasses and melts: a thermochemical model. *Chemical Geology*, 174, 157-179.
- 1219 Palme, H., & O'Neill, H.St.C. (2014), Cosmochemical estimates of mantle composition. In:  
1220 Treatise on Geochemistry, 2<sup>nd</sup> Edition, Chapter 3.1, 1-39.
- 1221 Papike, J.J., Karner, J.M., & Schearer, C.K. (2005). Comparative planetary mineralogy: Valence  
1222 state partitioning of Cr, Fe, Ti, and V among crystallographic sites of olivine, pyroxene, and  
1223 spinel from planetary basalts. *American Mineralogist*, 90, 277-290.
- 1224 Papike, J.J., Burger, P.V., Bell, A.S., Shearer, C.K., Le, L., & Jones, J. (2015). Normal to inverse  
1225 transition in martian spinel: Understanding the interplay between chromium, vanadium, and  
1226 iron valence state partitioning through a crystal-chemical lens. *American Mineralogist*, 100,  
1227 2018-2025.
- 1228 Papike, J.J., Simon, S.B., Burger, P.V., Bell, A.S., Shearer, C.K., & Karner, J.M. (2016). Chromium,  
1229 vanadium, and titanium valence systematics in Solar System pyroxene as a recorder of  
1230 oxygen fugacity, planetary provenance, and processes. *American Mineralogist*, 101, 907-918.
- 1231 Park, J.W., Kamenetsky, V., Campbell, I., Park, G., Hanski, E., & Pushkarev, E. (2017). Empirical  
1232 constraints on partitioning of platinum group elements between Cr-spinel and primitive  
1233 terrestrial magmas. *Geochimica et Cosmochimica Acta*, 216, 393-416.
- 1234 Pedersen, A.K. (1981). Armalcolite-bearing Fe-Ti oxide assemblages in graphite-equilibrated  
1235 sialic volcanic rocks with native iron from Disko, central West Greenland. *Contributions to*  
1236 *Mineralogy and Petrology*, 77, 307-324.

- 1237 Peters, M.T., Shaffer, E.E., Burnett, D.S., & Kim, S.S. (1995). Magnesium and titanium partitioning  
1238 between anorthite and Type B CAI liquid: Dependence on oxygen fugacity and liquid  
1239 composition. *Geochimica et Cosmochimica Acta*, 59, 2785-2796.
- 1240 Phinney, W.C. (1992). Partition coefficients for iron between plagioclase and basalt as a function  
1241 of oxygen fugacity: Implications for Archean and lunar anorthosites. *Geochimica et*  
1242 *Cosmochimica Acta*, 56, 1885-1895.
- 1243 Popp, R.K., Virgo, D., Yoder, H.S., Hoering, T.C. & Phillips, M.W. (1995). An experimental study of  
1244 phase equilibria and Fe oxy-component in kaersutitic amphibole: Implications for the fH<sub>2</sub>  
1245 and aH<sub>2</sub>O in the upper mantle. *American Mineralogist*, 80, 534-548.
- 1246 Poustovetov, A.A., & Roeder, P.L. (2000). The distribution of Cr between basaltic melt and  
1247 chromium spinel as an oxygen geobarometer. *Canadian Mineralogist*, 39, 309-317.
- 1248 Rhodes, J.M., & Vollinger, M.J. (2005). Ferric/ferrous ratios in 1984 Mauna Loa lavas: A  
1249 contribution to understanding the oxidation state of Hawaiian magmas. *Contributions to*  
1250 *Mineralogy and Petrology*, 149, 666-674.
- 1251 Righter, K. & Shearer C.K. (2003). Magmatic fractionation of Hf and W: Constraints on the timing  
1252 of core formation and differentiation in the Moon and Mars. *Geochimica et Cosmochimica*  
1253 *Acta*, 67, 2497-2507.
- 1254 Righter, K., Sutton, S.R., Newville, M., Le, L., Schwandt, C.S., Uchida, H., Lavina, B., & Downs, R.T.  
1255 (2006a). An experimental study of the oxidation state of vanadium in spinel and basaltic  
1256 melt with implications for the origin of planetary basalt. *American Mineralogist*, 91, 1643-  
1257 1656.
- 1258 Righter, K., Leeman, W.P., & Hervig, R.L. (2006b). Partitioning of Ni, Co and V between spinel-  
1259 structured oxides and silicate melts: Importance of spinel composition. *Chemical Geology*,  
1260 227, 1-25.
- 1261 Righter, K., Sutton, S., Danielson, L., Pando, K., Schmidt, G., Yang, H., Berthet, S., Newville, M.,  
1262 Choi, Y., Downs, R.T., & Malavergne, V. (2011). The effect of fO<sub>2</sub> on the partitioning and  
1263 valence of V and Cr in garnet/melt pairs and the relation to terrestrial mantle V and Cr  
1264 content. *American Mineralogist*, 96, 1278-1290.
- 1265 Righter, K., Danielson, L.R., Pando, K.M., Shofner, G.A., Sutton, S.R., Newville, M., & Lee, C.T.  
1266 (2016). Valence and metal/silicate partitioning of Mo: implications for conditions of Earth  
1267 accretion and core formation. *Earth and Planetary Science Letters*, 437, 89-100.
- 1268 Roeder, P.L. & Reynolds, I. (1991). Crystallization of chromite and chromium solubility in  
1269 basaltic melts. *Journal of Petrology*, 32, 909-934.
- 1270 Sato, M. (1978). Oxygen fugacity of basaltic magmas and the role of gas-forming elements.  
1271 *Geophysical Research Letters*, 5, 447-449.
- 1272 Schärer, U., Berndt, J. & Deutsch, A. (2011). The genesis of deep-mantle xenocrystic zircon and  
1273 baddeleyite megacrysts (Mbuji-Mayi kimberlite): Trace-element patterns. *European Journal*  
1274 *of Mineralogy*, 23, 241-255.
- 1275 Schreiber, H.D. (1977). Redox states of Ti, Zr, Hf, Cr, and EU in basaltic magmas-an experimental  
1276 study. Lunar and Planetary Science Conference Proceedings 8, 1785-1807.
- 1277 Schreiber, H.D. (1983). The chemistry of uranium in glass-forming aluminosilicate melts.  
1278 *Journal of the Less Common Metals*, 91, 129-147.
- 1279 Schreiber, H.D., & Haskin, L.A. (1976). Chromium in basalts: Experimental determination of  
1280 redox states and partitioning among synthetic silicate phases. 7th Lunar and Planetary  
1281 Science Conference, 1221-1259.

- 1282 Schreiber, H.D., Merkel, R.C., Schreiber, L.V., & Balazs, G.B. (1987). Mutual interactions of redox  
1283 couples via electron exchange in silicate melts: Models for geochemical systems. *Journal of*  
1284 *Geophysical Research*, 92, 9233-9245.
- 1285 Shannon, R.D. (1976). Revised effective ionic radii and systematic studies of inter-atomic  
1286 distance in halides and chalcogenides. *Acta Crystallographica*, 32, 751–767.
- 1287 Shearer, C.K., McKay, G., Papike, J.J., & Karner, J.M. (2006). Valence state partitioning of  
1288 vanadium between olivine-liquid: Estimates of the oxygen fugacity of Y980459 and  
1289 application to other olivine-phyric martian basalts. *American Mineralogist*, 91, 1657-1663.
- 1290 Shim, S-H., Grocholski, B., Ye, Y., Alp, E.E., Xu, S., Morgan, D., Meng, Y., & Prakapenka, V.B. (2017).  
1291 Stability of ferrous-iron-rich bridgmanite under reducing midmantle conditions. *PNAS*, 114,  
1292 6468-6473.
- 1293 Sievwright, R.H., Wilkinson, J.J., O'Neill, H.St.C., & Berry, A.J. (2017). Thermodynamic controls on  
1294 element partitioning between titanomagnetite and andesitic-dacitic melts. *Contributions to*  
1295 *Mineralogy and Petrology*, 172, 62.
- 1296 Simon, S.B., & Sutton, S. R. (2018). Valences of Ti, Cr, and V in Apollo 17 high-Ti and very low-Ti  
1297 basalts and implications for their formation. *Meteoritics & Planetary Science*, 53, 2138-2154.
- 1298 Smythe, D.J., & Brenan, J.M. (2015). Cerium oxidation state in silicate melts: Combined  $fO_2$ ,  
1299 temperature and compositional effects. *Geochimica et Cosmochimica Acta*, 170, 173-187.
- 1300 Smythe, D.J., & Brenan, J.M. (2016). Magmatic oxygen fugacity estimated using zircon-melt  
1301 partitioning of cerium. *Earth and Planetary Science Letters*, 453, 260-266.
- 1302 Sommer, J. (2014). Experimental study: Solubility of Pt and Rh in silicate melt as a function of  
1303 silicate melt compositions, temperature and oxygen fugacity. MSc Thesis, University of Bonn,  
1304 Germany.
- 1305 Sun, C.-O., Williams, R.J., & Sun, S.-S. (1974). Distribution coefficients of Eu and Sr for  
1306 plagioclase-liquid and clinopyroxene-liquid equilibria in oceanic ridge basalt: An  
1307 experimental study. *Geochimica et Cosmochimica Acta*, 38, 1415–1433.
- 1308 Sutton, S.R., & Newville, M. (2014). Synchrotron x-ray spectroscopic analysis. In: Treatise on  
1309 Geochemistry, 2<sup>nd</sup> Edition, H. Holland and K. Turekian (eds.), v. 15, p. 213-230.
- 1310 Sutton, S.R., Goodrich, C.A., & Wirick, S. (2017). Titanium, vanadium and chromium valences in  
1311 silicates of ungrouped achondrite NWA 7325 and ureilite Y-791538 record highly-reduced  
1312 origins. *Geochimica et Cosmochimica Acta*, 204, 313-330.
- 1313 Sutton, S.R., Karner, J., Papike, J., Delaney, J.S., Shearer, C., Newville, M., Eng, P., Rivers, M., & Dyar,  
1314 M.D. (2005). Vanadium K edge XANES of synthetic and lunar basaltic glasses and application  
1315 to microscale oxygen barometry. *Geochimica et Cosmochimica Acta*, 69, 2333-2348.
- 1316 Thomson, A.R., Kohn, S.C., Bulanova, G.P., Smith, C.B., Araujo, D., & Walter, M.J. (2016). Trace  
1317 element composition of silicate inclusions in sub-lithospheric diamonds from the Juina-5  
1318 kimberlite: Evidence for diamond growth from slab melts. *Lithos*, 265, 108-124.
- 1319 Toplis, M.J., & Corgne, A. (2002). An experimental study of element partitioning between  
1320 magnetite, clinopyroxene and iron-bearing silicate liquids with particular emphasis on  
1321 vanadium. *Contributions to Mineralogy and Petrology*, 144, 22-37.
- 1322 Trail, D., Watson, E.B., & Tailby, N.D. (2011). The oxidation state of Hadean magmas and  
1323 implications for early earth's atmosphere. *Nature*, 480, 79-82.
- 1324 Trail, D., Watson, E.B., & Tailby, N.D. (2012). Ce and Eu anomalies in zircon as proxies for the  
1325 oxidation state of magmas. *Geochimica et Cosmochimica Acta*, 97, 70-87.

- 1326 van Kan Parker, M., Mason, P.R.D. & van Westrenen, W. (2011). Experimental study of trace  
1327 element partitioning between lunar orthopyroxene and anhydrous silicate melt: Effects of  
1328 lithium and iron. *Chemical Geology*, 285, 1-14.
- 1329 Wade, J., Wood, B.J., & Norris, A. (2013). The oxidation state of tungsten in silicate melt at high  
1330 pressures and temperatures. *Chemical Geology*, 335, 189–193.
- 1331 Wade, J., Wood, B.J., & Tuff, J. (2012). Metal–silicate partitioning of Mo and W at high pressures  
1332 and temperatures: evidence for late accretion of sulphur to the Earth. *Geochimica et*  
1333 *Cosmochimica Acta*, 85, 58-74.
- 1334 Wadhwa, M. (2008). Redox conditions on small bodies, the Moon and Mars. *Reviews in*  
1335 *Mineralogy and Geochemistry*, 68, 493-510.
- 1336 Wijbrans, C.H., Klemme, S., Berndt, J., & Vollmer, C. (2015). Experimental determination of trace  
1337 element partition coefficients between spinel and silicate melt: The influence of chemical  
1338 compositions and oxygen fugacity. *Contributions to Mineralogy and Petrology*, 169, 45.
- 1339 Wilke, M., & Behrens, H. (1999). The dependence of the partitioning of iron and europium  
1340 between plagioclase and hydrous tonalitic melt on oxygen fugacity. *Contributions to*  
1341 *Mineralogy and Petrology*, 137, 102-114.
- 1342 Wood, B.J., & Blundy, J.D. (2003). Trace element partitioning under crustal and upper mantle  
1343 conditions: The influences of ionic radius, cation charge, pressure, and temperature. In:  
1344 *Treatise on Geochemistry*, vol. 2, chapter 2.09, R.W Carlson (Ed.), p. 395-424.
- 1345 Woodhead, J.D. (1989). Geochemistry of the Mariana arc (western Pacific): Source composition  
1346 and processes. *Chemical Geology*, 76, 1-24.
- 1347 Young, E.D., Dyl, K.A., & Simon, J.I. (2012). Response to the Comment by SB Simon, L. Grossman,  
1348 and SR Sutton on “Valence state of titanium in the Wark-Lovering rim of a Leoville CAI as a  
1349 record of progressive oxidation in the early Solar Nebula”. *Geochimica et Cosmochimica Acta*,  
1350 85, 377-382.

1351  
1352

### 1353 Figure captions

1354

1355 **Figure 1. (a)** Schematic illustration of lattice strain parameters  $D_0$ ,  $r_0$  and  $E$  for the mineral/melt  
1356 partition coefficient ( $D$ ) of an element  $i$  as modelled by the Brice equation (Blundy and Wood,  
1357 1994);  $D_i = D_0 \exp([-4\pi EN_A(r_0 - r_i)^2 - 1/3(r_0 - r_i)^3]/RT)$ , and **(b, c, d)** measured changes in  
1358 these parameters with cation valence state (i.e. charge) as determined experimentally for  
1359  $\text{CaSiO}_3$ /melt partitioning (Law et al., 2000).  
1360

1361 **Figure 2.** Relative oxygen fugacity conditions (in log units relative to FMQ, the fayalite-  
1362 magnetite-quartz buffer; values from O'Neill, 1987) for several planetary geochemical  
1363 reservoirs (Frost and McCammon, 2008; Grossman et al. 2008; Wadhwa, 2008), and valence  
1364 state transition ranges for the elements discussed in this chapter. See text for references. Also  
1365 plotted for reference the IW (Fe-FeO), NNO (Ni-NiO), and HM (hematite-magnetite) buffers.  
1366

1367 **Figure 3:** Mineral/melt partitioning of transition metals as a function of oxygen fugacity (in log  
1368 units relative to FMQ, the fayalite-magnetite-quartz buffer; values from O'Neill, 1987) for  
1369 selected minerals. Abbreviations: amph - amphibole, cpx - clinopyroxene, opx - orthopyroxene,  
1370 olv - olivine, plag - plagioclase feldspar, spl - spinel, zrc - zircon. All curves shown in the main  
1371 diagram are best fits of the experimental data to an equation with the same form as Equation  
1372 22. The fraction (from 0 to 1) of the different valence states of each element are plotted on top  
1373 of the diagram. These were calculated using Equation 13 using available data. **(a)** Fe  
1374 mineral/melt partitioning data from King et al., 2000 (amph), Mallmann and O'Neill, 2009 (spl),

1375 olv, opx, cpx) and Phinney, 1992 (plag). **(b)** Cr mineral/melt partitioning data from Mallmann  
 1376 and O'Neill, 2009 (olv, opx, cpx). **(c)** Ti mineral/melt partitioning data from Mallmann and  
 1377 O'Neill, 2009 (olv, opx, cpx), Peters et al. 1995 (plag) and Burnham and Berry, 2012 (zrc). **(d)**  
 1378 (d) V mineral/melt partitioning data from Mallmann and O'Neill, 2009 (olv, opx, cpx, spl).  
 1379

1380 **Figure 4.** Comparison of Cr olivine( $\text{Fo}_{100}$ )/melt partitioning coefficients obtained at 1 bar and  
 1381 1320 °C as a function of oxygen fugacity (in log units relative to FMQ, the fayalite-magnetite-  
 1382 quartz buffer; values from O'Neill, 1987) for three Fe-free compositions in the CaO-MgO- $\text{Al}_2\text{O}_3$ -  
 1383  $\text{SiO}_2$  system: FAS1, FAD1 and FAD3 (Hanson and Jones, 1998). The results illustrate a mild effect  
 1384 of melt composition on the partitioning of  $\text{Cr}^{3+}$  yet no significant effect on the partitioning of  
 1385  $\text{Cr}^{2+}$ . The fraction (from 0 to 1) of the different valence states are plotted on top of the diagram.  
 1386

1387 **Figure 5.** Zircon/melt partition coefficients for REE elements determined experimentally at 1  
 1388 bar as a function of oxygen fugacity by Burnham and Berry (2012). The colored segments  
 1389 highlight systematic changes in the partitioning of Ce and Eu with oxygen fugacity (labelled  
 1390 relative to the FMQ buffer).  
 1391

1392 **Figure 6.** Mineral/melt partitioning of redox-sensitive rare earth elements (REE), Ce **(a)** and Eu  
 1393 **(b)** as a function of oxygen fugacity (in log units relative to FMQ, the fayalite-magnetite-quartz  
 1394 buffer; values from O'Neill, 1987) for selected minerals. Abbreviations: bdd - baddeleyite, cpx -  
 1395 clinopyroxene (aluminous diopside), olv - olivine, opx - orthopyroxene, plag - plagioclase  
 1396 feldspar, ttn - titanite, zrc - zircon. Where data were not obtained as a function of  $f\text{O}_2$ , partition  
 1397 coefficients for  $\text{Ce}^{3+}$ ,  $\text{Ce}^{4+}$ ,  $\text{Eu}^{2+}$  and  $\text{Eu}^{3+}$  (or estimates thereof) were used in conjunction with  
 1398 the  $\text{Ce}^{4+}/\Sigma\text{Ce}$  and  $\text{Eu}^{3+}/\Sigma\text{Eu}$  models of Burnham and Berry (2014) and Burnham et al. (2015).  
 1399 Data from Klemme and Meyer, 2003 (bdd), Leitzke et al., 2017 (cpx-Ce, plag-Ce, olv), Sun et al.,  
 1400 1974 (cpx-Eu, plag-Eu, opx-Eu), van Kan Parker et al., 2011 (opx-Ce), Bachmann et al., 2005  
 1401 (ttn), and Burnham and Berry, 2012 (zrc). See Fig. 3 for more details.  
 1402

1403 **Figure 7.** Mineral/melt partitioning of U as a function of oxygen fugacity (in log units relative to  
 1404 FMQ, the fayalite-magnetite-quartz buffer; values from O'Neill, 1987) for selected minerals.  
 1405 Abbreviations: cpx - clinopyroxene (diopside), olv - olivine, opx - orthopyroxene, zrc - zircon.  
 1406 Data from Fonseca et al., 2014 (opx, cpx, olv), and Burnham and Berry, 2012 (zrc). See Fig. 3 for  
 1407 more details.  
 1408

1409 **Figure 8.** Mineral/melt partitioning of siderophile elements (Mo, W and Re) as a function of  
 1410 oxygen fugacity (in log units relative to FMQ, the fayalite-magnetite-quartz buffer; values from  
 1411 O'Neill, 1987) for selected minerals. Abbreviations: cpx - clinopyroxene, opx - orthopyroxene,  
 1412 olv - olivine, spl - spinel, grt - garnet. Data from Leitzke et al., 2017 (Mo: cpx, opx, olv), Wijbrans  
 1413 et al., 2015 (Mo: spl), Fonseca et al., 2014 (W: opx, cpx, olv), and Mallmann and O'Neill, 2007  
 1414 (Re: cpx, opx, spl, grt, ol). See Fig. 3 for more details.

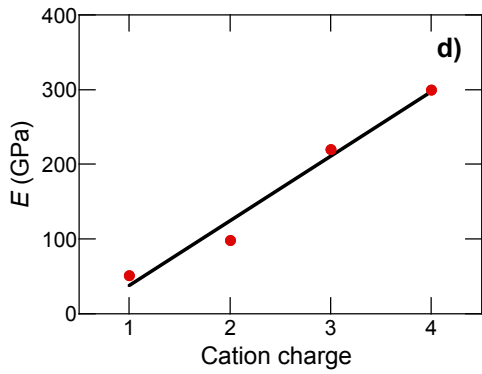
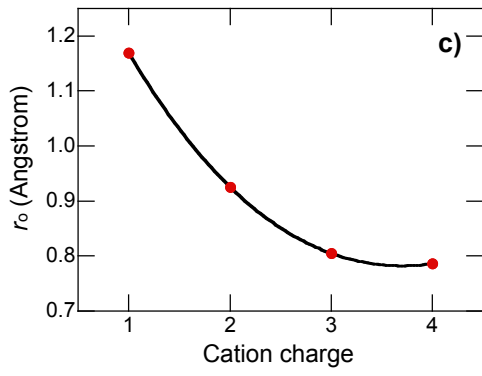
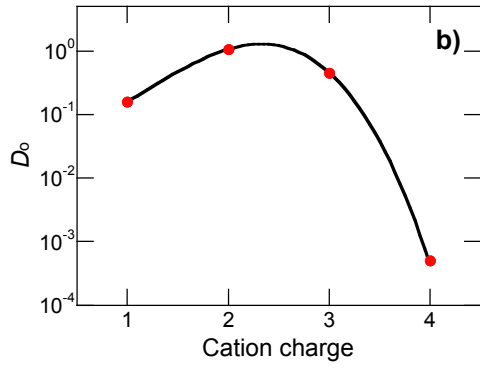
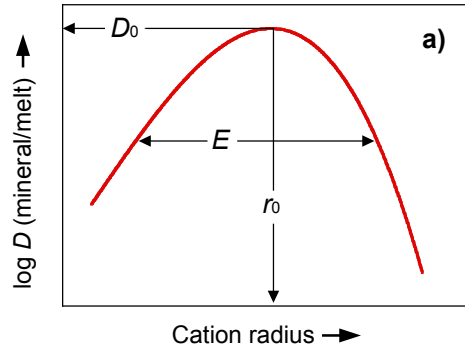


Figure 2

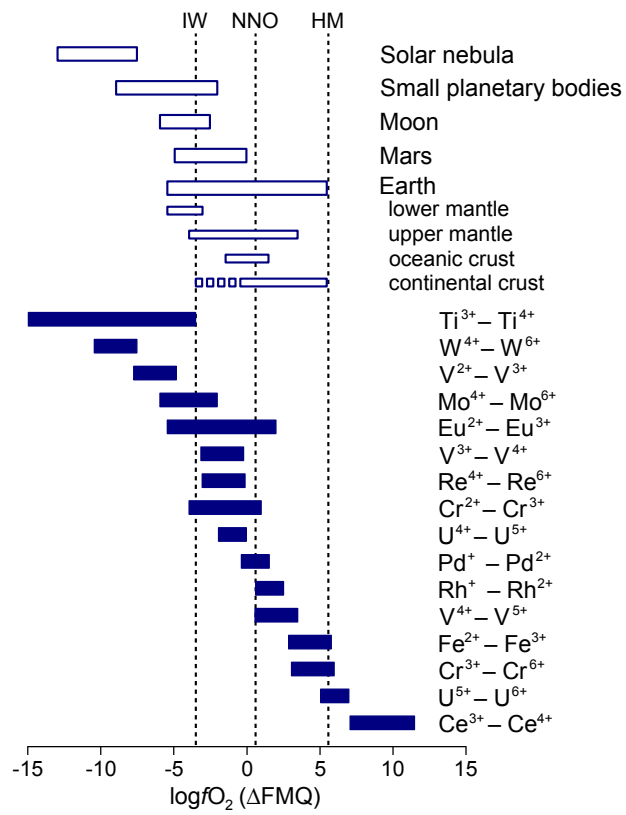


Figure 3

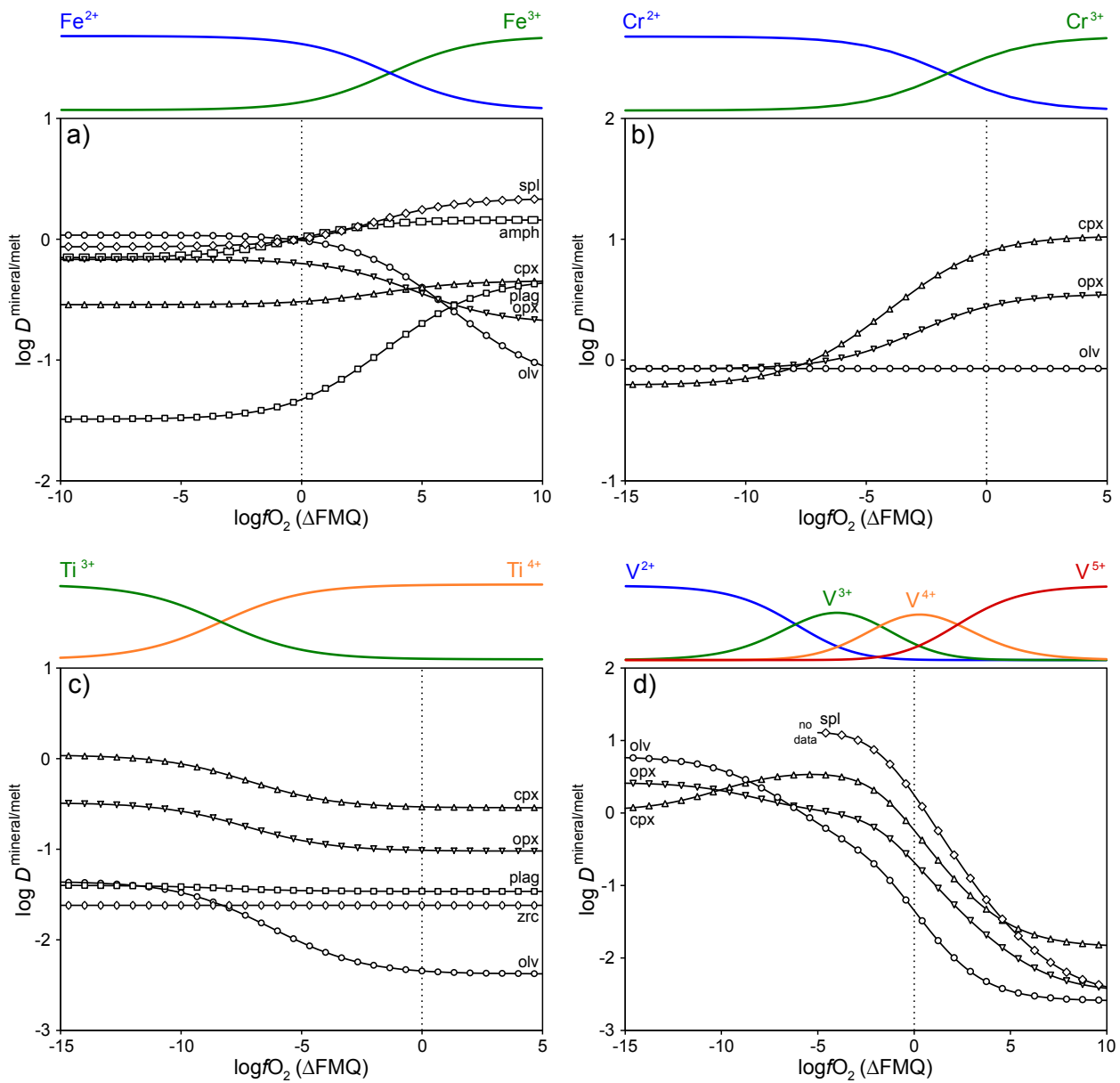


Figure 4

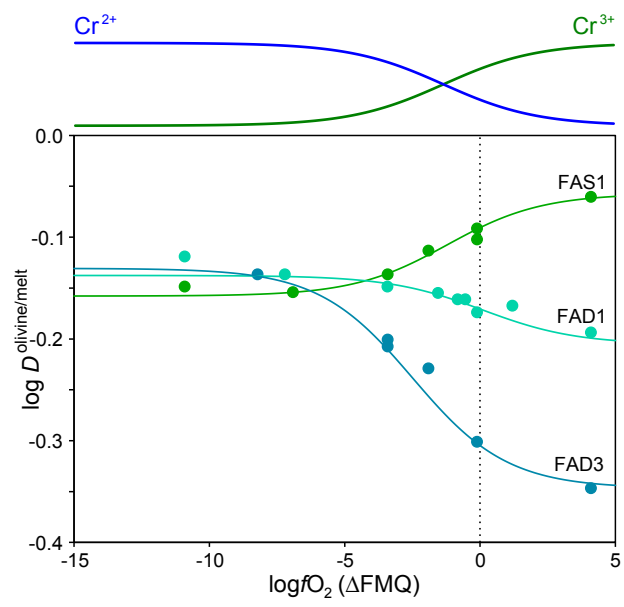


Figure 5

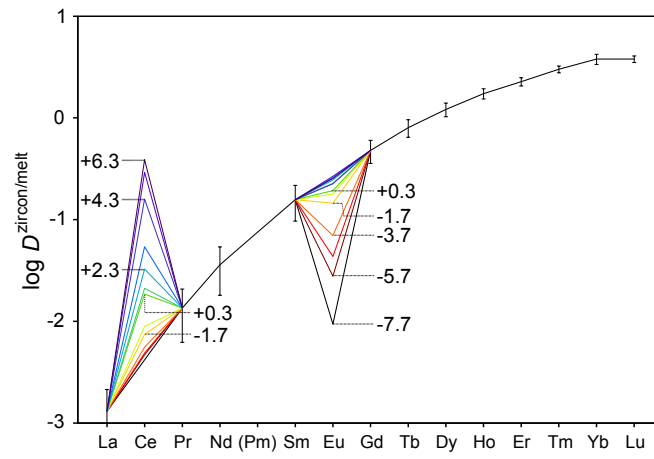


Figure 6

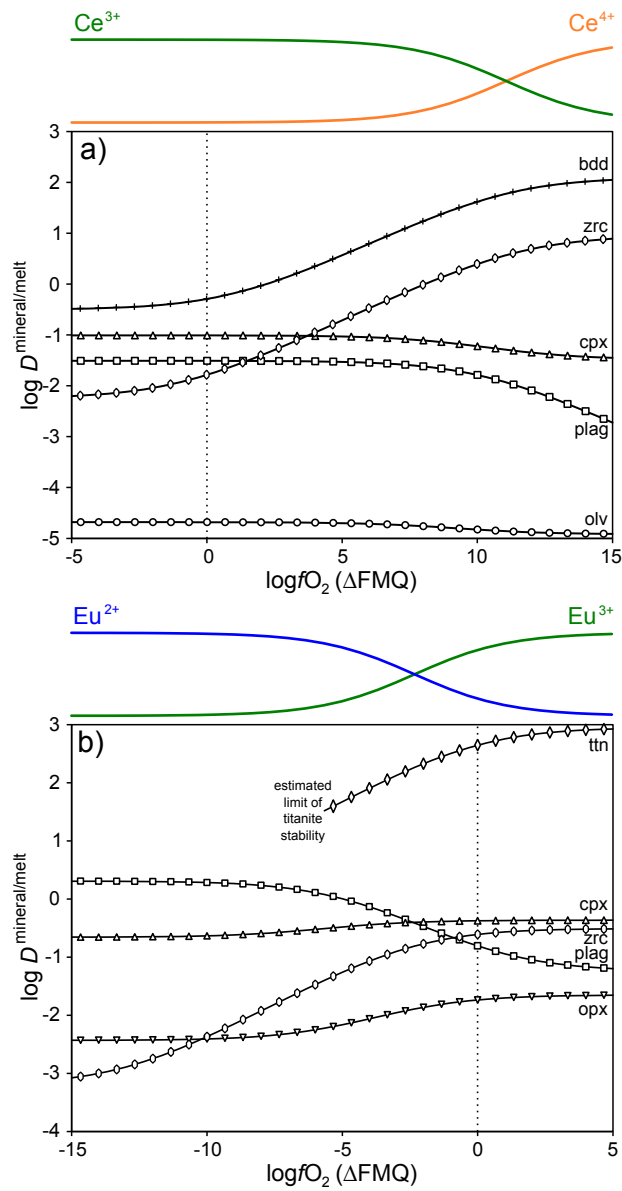


Figure 7

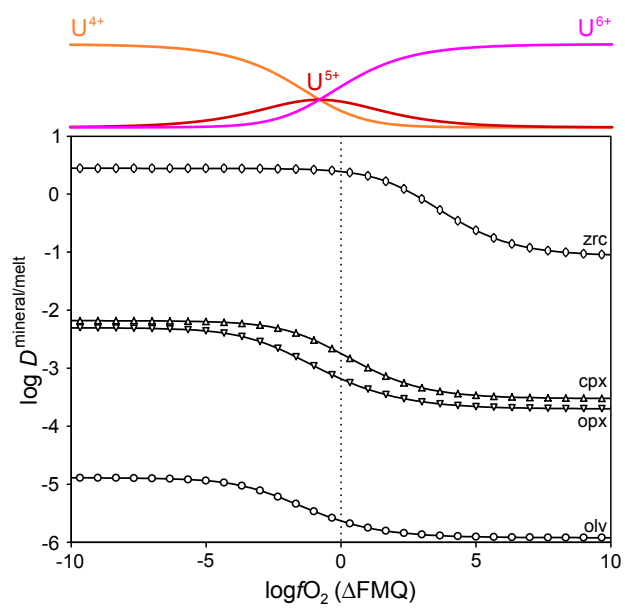


Figure 8

